SCUOLA DI DOTTORATO
UNIVERSITÀ DEGLI STUDI DI MILANO-BICOCCA

Dipartimento di / Department of

Fisica "G. Occhialini"

Dottorato di Ricerca in / PhD program PHYSICS and ASTRONOMY Ciclo / Cycle XXXI

Curriculum in (se presente / if it is) Subnuclear Physics and Physical Technologies

Oscillator-Based CMOS Readout Interfaces for Gas Sensing Applications

Cognome / Surname CICIOTTI Nome / Name FULVIO

Matricola / Registration number 787101

Tutore / Tutor: Prof. Massimo GERVASI

Supervisor: Prof. Andrea BASCHIROTTO
(se presente / if there is one)

Coordinatore / Coordinator: Prof. Marta CALVI

ANNO ACCADEMICO / ACADEMIC YEAR 2017/2018

Fulvio Ciciotti: *Oscillator-Based CMOS Readout Interfaces for Gas Sensing Applications* | Ph.D Thesis in Physics and Astronomy, Università Milano-Bicocca.

Abstract

Detection of toxic and dangerous gases has always been a need for safety purpose and, in recent years, portable and low-cost gas sensing systems are becoming of main interest. This thesis presents fast, high precision, low-power, versatile CMOS interface circuits for portable gas sensing applications. The target sensors are Metal Oxide Semiconductor (MOX) sensors which are widely used due to their inherent compatibility with integrated MEMS technologies. The chosen readout typologies are based on the time-domain Resistor-Controlled Oscillator. This guarantees wide dynamic range, good precision and the ability to cope with the large MOX sensor resistance variations. Four different prototypes have been successfully developed and tested. Chemical measurements with a real SnO_2 MOX sensor have also been performed to validate the results, showing a minimum CO detection capability in ambient air of 5 ppm. The ASICs are able to cover 128 dB of DR at 4 Hz of digital output data rate, or 148 dB at 0.4 Hz, while providing a relative error always better than 0.4 % (SNDR $\geq$ 48 dB). Target performances have been achieved with aggressive design strategies and system-level optimization, and using a scaled (compared to typical implementations in this field) 130 nm CMOS technology provided by Infineon Technologies AG. Power consumption is about 450 µA. Moreover, this work introduces the possibility to use the same oscillator-based architecture to perform capacitive sensors readout. Measurement results with capacitive MEMS sensors have shown 116 dB of DR in C_{SENS} mode, with an SNR of 74 dB at 10 Hz of digital output data rate. The architectures developed in this thesis are compatible with the modern standards in the portable gas sensing industry.

Keywords: gas sensors, MOX, resistance-to-frequency, MEMS, capacitance sensors, readout interfaces, low-power

Contents

List of Figures

List of Tables

Introduction

This Ph.D Thesis summarizes the research activities on developing CMOS readout interfaces for gas sensing applications for portable devices. This work has been carried out in a collaboration between the microelectronic group of the University of Milano-Bicocca and the RF & Sensor department of Infineon Technologies AG in Villach (Austria).

The thesis is outlined as follows:

In the first chapter a general overview of gas sensing micro-systems is presented. This chapter describes the motivations behind the research activity and the aims of this work. After a brief description of gas sensors and the physical principles behind their functioning, several state-of-the-art readout circuits are reviewed.

In the second chapter a theoretical analysis of the chosen readout topology is addressed, including non-ideal behaviors. Then a Matlab-Simulink model is used for design optimization and performances analysis.

In the third chapter the first prototype developed, UB01, is discussed. First, details of the CMOS implementations are described and explained, then the most relevant simulation results are presented. This chapter also includes electrical and chemical characterization of the prototype, including descriptions of the measurement setup.

The fourth chapter focuses on improvements of the first test-chip. These improvements concern performances and the possibility to adapt the interface to different sensors specifications and/or multiplexing capabilities. Moreover the same readout approach is extended to be able to perform capacitive measurement using the same basic principle of the resistance readout. These considerations led to the production of three other test-chips, UB31, UB32 and UB33. Simulations results and measurements of these prototypes are here discussed.

The last chapetr summarizes the most relevant results obtained from the research activity and provides a comparison with the state-of-the-art.

Chapter 1

Gas Sensing Systems Overview

1.1 Introduction

Gas sensors have always played a key role in many applications, such as automotive, industrial control, medical care, indoor and environmental air quality control, and these demands have led to the development of a number of different sensor technologies. Traditional gas analysis methods, based on gas chromatography (GC), mass spectrometry (MS) and Fourier transform infrared (FT-IR) spectrometry, are complex and expensive, suitable to operate in fixed locations and buildings. The increasing attention to air quality and safety standards of recent years, however, requires the development of portable, low-cost gas sensing systems for consumer applications [1] [2]. These electronic noses or *e-noses* should be small enough to be integrated in portable personal devices such as smartphones, have low power consumption to preserve battery life and exhibit sufficiently long lifetime (5-10 years). Moreover they must satisfy modern standards for air quality monitoring [3] [4] leading to engineering challenges for sensor, electronic interface and data processing unit development. Indeed an e-nose system is composed by these three main parts: the sensing element or the array of sensors, to physically detect target gases, the electronic interface circuit for the sensor readout and the data processing unit to collect data and perform the final gas recognition. Among the different technologies for the sensing element, Metal Oxide Semiconductor (MOX) sensors are the most promising due to their good performances and inherent compatibility with integrated CMOS technologies [5] [6], which are used for the electronic interface and for the data processing unit. This potentially allow the integration of sensor and interface in the same small packages.

Full CMOS integration however, is not yet widely adopted. MOX sensors are compatible but several challenges are still present [7]. They require high operative temperature (around 300 °C - 400 °C) that must be reached with embedded integrated heaters, while typical CMOS silicon substrates cannot exceed 120 °C. Thermal isolation between sensor and ASIC must be then carefully evaluated, especially in a monolithic approach where sensor and interface coexist on the same die. The high temperature requirement makes also achieving low power consumption very critical, even if last nanotechnologies improvements allow fabrication of micro-machined embedded low-power heater/thermometer small enough to reach the operating temperature in few tens of milliseconds [8] [9] [10]. Today's semiconducting sensing materials have sufficiently small size, low weight, and modest power requirements. Although there has been a significant improvement in minimizing undesired effect such as high cross-sensitivity, sensitivity to humidity, long-term signal drift and slow sensor response, high performances CMOS interfaces are still needed to perform precise readout and final gas recognition. Indeed a combined effort between sensor and readout development is mandatory to ensure optimal results.

This work will be focused on the realization of low-cost, high performances CMOS readout interfaces compatible with the recent standards and requirements in the gas sensing industry.

1.2 MOX sensors

The history of chemoresistive gas sensors begins more than sixty years ago when was first demonstrated that some semiconductor materials, such as Ge, modify their resistance depending on the presence of impurities in its volume or at the surface [11]. Later it was shown that ZnO thin films heated at high temperatures exhibit conductivity variations in the presence of traces of reactive gases in the air [12]. After that several metal oxides have been investigated and among them tin dioxide (SnO_2) turns out to be one of the most advantageous in term of sensitivity, operative temperature and overall stability [13].

Today, thanks to the new opportunities provided by nanoscale technologies, is it possible to develop much better performing semiconducting sensing materials. The new sensors have substantially smaller size, lower weight, and more modest power

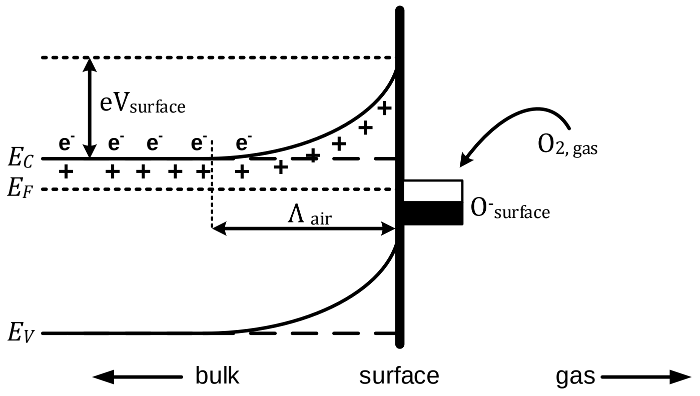

Figure 1.1: Simplified model of band bending in a wide-bandgap semiconductor. E_C, E_V and E_F are energy of conduction band, valence band and Fermi level. e^- represent conductin electrons and + donor sites (adapted from [15])

requirements. Moreover there has been a significant improvement in minimizing undesired effects such as high cross-sensitivity, sensitivity to humidity, long-term signal drift and slow sensor response.

1.2.1 Sensing Principle

The working principle of a typical MOX gas sensor essentially consists in the change of electrical properties of the metal-oxide semiconductor due to the interaction between gas molecules and the surface of the sensor itself [14] [15]. The state of equilibrium at the sensor surface depends on the reaction between the surface oxygen and the surrounding air. The presence of target gas analyte changes the rates of chemisorbed oxygen essentially causing a variation of the resistance of the sensor material.

In Figure 1.1 a schematic diagram of band bending after chemisorptions in a wide-bandgap semiconductor is reported. O_2 molecules, when absorbed, extract electrons from the conduction band E_C and trap them on the surface in the form of ions, leading to a band bending and the creation of an electron-depleted region called space-charge layer. The thickness of this region (Λ_{air}) corresponds with the length of the band bending region. The band bending generates also a surface potential barrier $eV_{surface}$. Height and depth of the band bending depend on the amount and type of absorbed oxygen causing the surface charge, and obviously on the characteristics of the semiconducting material used (Debye lenght,

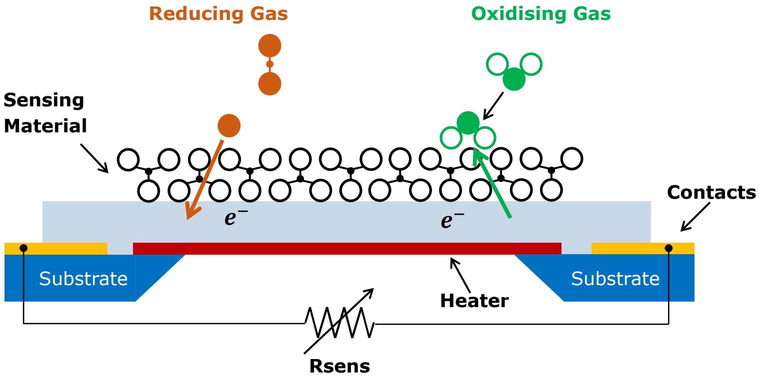

Figure 1.2: MOX sensor cross-section

donor concentration, ..). When the reaction of these oxygen species with reducing gases occurs, the band bending decreases and can even be reversed, resulting in an increased conductivity. Also temperature plays a major role in this process. Oxygen is ionosorbed predominantly as O^- for temperatures in the 300 °C to 450 °C range and this increases sensitivity significantly [16] thus typically MOX sensors operate in that temperatures range.

The simplified band bending model described above, works only for n-type semiconducting metal oxides (e.g. SnO_2) with depletion regions smaller than their grain size and in complete absence of humidity, which also strongly affects MOX sensitivity and performances [14]. There are many other mechanisms behind the sensing principle and even a complete knowledge of the surface chemistry involved in the gas detection may not be enough to fully understand the dependence of the sensor resistance on the gas pressure and concentration. For example, the sensing layer morphology plays a different role depending on the porosity of the layer itself. In compact layers the interaction takes place only at the geometric surface, while in porous layers also the volume is accessible to the gases, increasing the active surface, and electronic conductivity occurs also via grain-to-grain contacts.

A complete description of every mechanism behind the sensing principle is beyond this thesis purposes and a MOX sensor can be simplified as a variable resistor. In presence of reducing gases there is an increase of the conductivity if the MOX is an n-type semiconductor, and a decrease if is a p-type; whereas in presence of oxidizing gases the effect is reversed. A typical MOX gas sensor cross-section is reported in Figure 1.2. It is composed by the sensitive layer deposited on a silicon substrate, an embedded heater used to reach the high operative temperatures and contact electrodes to detect resistance variations.

1.2.2 Resistance Value

Even if exact mechanisms of MOX resistance variation due to the gas presence are not yet fully understood, it is still possible to estimate the magnitude of resistance variation (ΔR_{GAS}), which can be up to two-decades from the baseline resistance (R_{BASE}) of the sensor. Considering also that the baseline resistance is affected by fabrication process and technological spread, by environmental factors such as temperature and humidity, and by long term drift due to aging, is it clear that the overall sensor resistance may vary over several decades (Equation 1.1).

$$R_{SENS} = R_{BASE} + \Delta R_{BASE} + \Delta R_{GAS} \tag{1.1}$$

In early developed sensors the ratio between maximum and minimum R_{SENS} values could have been in the 10^5 or even 10^6 range, while today this number is decreased due to better fabrication process and overall sensor technologies. Nevertheless a dynamic range (DR) of about 4-decades is still mandatory for the readout circuit to cope with MOX sensors resistance variations and requirements imposed by the minimum resolvable resistance change.

1.2.3 Pattern Recognition Techniques and Gas Detection

One of the biggest shortcomings of MOX sensors is their inherent cross-sensitivity to the multitude of different gases that can react with the active surface, which makes selectivity to a single analyte particularly challenging. This creates the necessity to develop different methodologies to overcome the problem. Among the several approaches adopted, promising results have been achieved applying different temperature patterns on sensor arrays or even on a single sensor [17] [18] [19]. It is well known that MOX sensitivity is strongly correlated to the operative temperatures and that the optimal temperature is different for each analyte. Also, temperature modulation can produce gas dependent response patterns that change according to the way in which the operating temperature is varied. Modern micro-hotplates and heaters have thermal constants that allow fast heating cycles, which makes driving the sensors with a periodical and/or pulsed temperature waveform

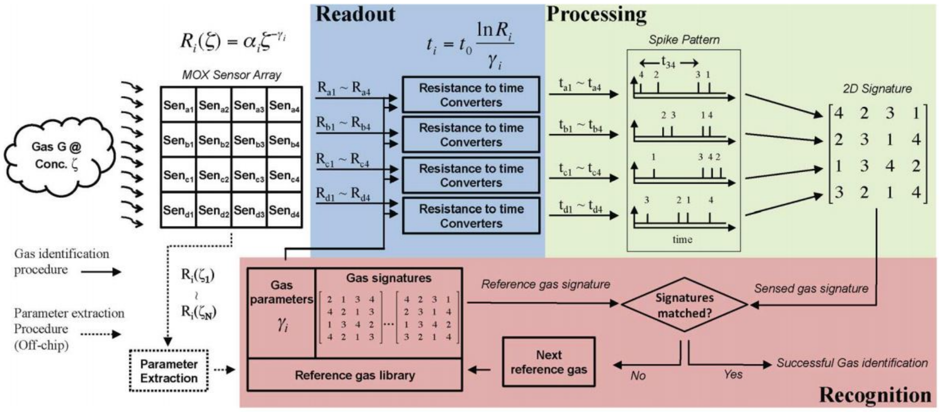

Figure 1.3: Example of gas sensing readout with pattern recognition circuit (adapted from [20])

possible. Moreover, it has been reported that important information on different gases can be extracted analyzing transient behavior even before sensor stabilization and performing complex pattern recognition technique [21]. Often such analysis are performed collecting data from a matrix of different sensors exposed to the analyzed air, to increase the number of useful data and information. In [22], a humidity–temperature correction model is presented, showing the importance to include humidity information in the gas discrimination analysis.

1.3 Readout Interface Circuits

1.3.1 Interface Requirements

Before discussing how CMOS readout architectures for MOX sensors can be implemented, it is important to remind readouts requirements dictated by sensors response behavior. The resistance to be detected ranges over several decades, as mentioned above, and the readout interface must be able to cover a large DR. Required measurement accuracy depends on the target application. For simple indoor detection of common gases (CO, NO_2, CH_4) precision of about 2 % is usually sufficient to guarantee detection in the few part per million (ppm) range. For outdoor gas detection and in presence of more analytes, the required precision must be higher (relative error in the measurement $< 0.5\,\%$). Moreover, the complex pattern recognition algorithms require sufficiently fast data rate to perform such complex analysis and a throughput better than 1 Hz is mandatory. Lastly, power consumption of the readout must be minimized, to allow integration in portable, battery-powered devices.

1.3.2 State-of-the-Art Overview

Many transducers, like MOX sensors, are based on the detection of a conductance variation, and interfaces for resistive sensors are widely discussed and adopted in literature [7] [23]. They can be summarized in three main categories:

- direct resistance-to-voltage conversion
- multi-scale or logarithmic compression
- resistance-to-frequency conversion

Direct Resistance-to-Voltage Conversion

The simplest way to detect an unknown resistance value is to perform resistive readout using a voltage divider or a Wheatstone bridge structure. Although very simple, these solutions are only suitable for relatively small resistance variations, and suffer from poor linearity when reaching the extremes of their already limited dynamic range. Even if different techniques can be used to improve linearity of bridges [24], and bridge structures have been employed in the past [25], they are clearly not a good choice considering the wide DR of MOX sensors. Moreover, technology scaling is compromising direct resistance-to-voltage conversion DR even more because of the lower and lower power supply.

Logarithmic Compression and Multi-scale

Logarithmic compression circuits are able to sustain much wider DR because of the compression obtained establishing a logarithmic relationship between input sensor resistance and output voltage. An example of a logarithmic compression circuit for MOX sensors [26] is reported in Figure 1.4. A Voltage-to-Current (V2I) converter is used to fed the sensor current to a couple of diodes implemented with two pnp transistors. The voltage compression is obtained exploiting the log scale in the diodes equation. However, the precision achieved is only about 2 %. These type of circuits suffer form mismatch between diodes and have a non-linear resistance-voltage relationship.

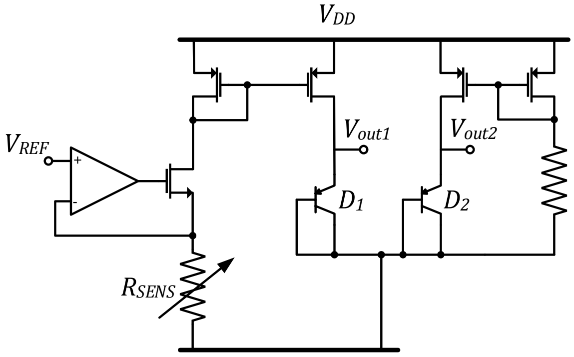

Figure 1.4: Logarithmic compression circuit (adapted from [26])

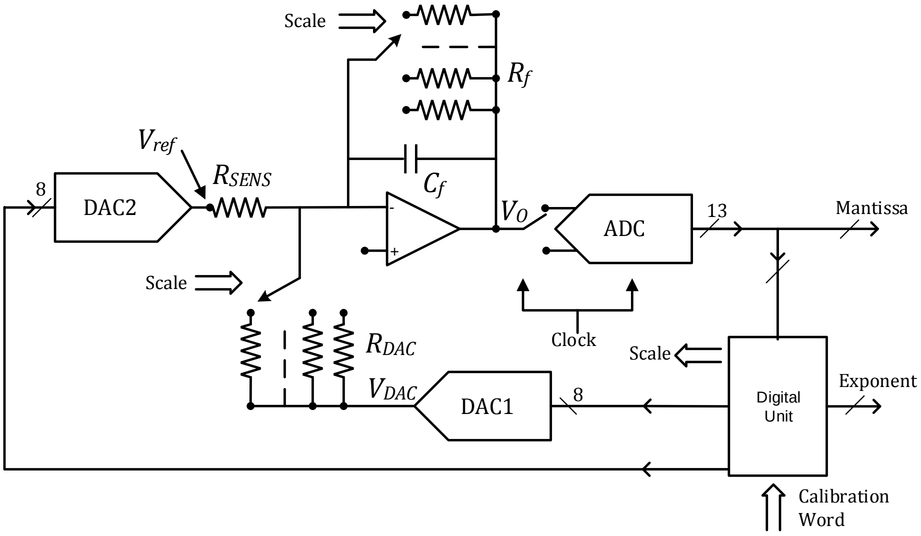

Figure 1.5: Multi-scale readout based on a programmable-gain amplifier and ADC (adapted from [27])

Another possible approach takes direct inspiration from laboratory equipment and instruments. The idea is to extend DR by using different conversion scales that overlap at their extremes. This *multimeter-style* technique allows a very large DR with excellent precision but requires complex control logic to implement the auto-ranging function and to calibrate possible discontinuities among the different scales. In Figure 1.5 an example of a multi-scale readout is reported [27]. A trans-resistance amplifier is used in combination with an ADC. The multi-scale

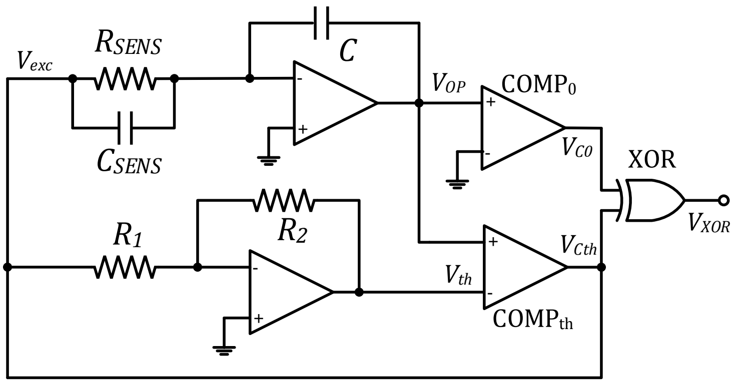

Figure 1.6: Oscillator-based readout with MOX sensor inside the oscillating circuit (adapted from [28])

functionality is implemented acting on the gain of the amplifier, by selecting different feedback resistors from an array. A programmable subtracting current is also used to compensate output voltage inaccuracy. The solution achieves an impressive 160 dB of DR guaranteeing over 12 bits of effective relative resolution. However, the very complex architecture and control logic, implemented with a DSP, consumes more than 15 mW and is not very suitable for cheap, low-power devices.

Oscillator-based Readout

Oscillator-based readouts operate shifting in the time domain the large DR problem, thus avoiding limitations imposed by voltage swing constraints. The resistance-to-frequency conversion can be obtained exploiting an oscillator circuit, with oscillation frequencies proportional to the sensor resistance. Different oscillator-based readouts reported in literature are able to cover very wide DR with good linearity, but they usually achieve poor output data rate, since they trade off conversion time for resolution and DR [29] [30]. Moreover, most of the proposed oscillator-based architectures focus only on achieving high precision and DR, often overlooking the digital conversion of the oscillation frequency, or simply using expensive micro-controllers for signal processing, increasing costs and power consumption [28] [30] [31] [32]. Oscillator-based circuits can be divided in two categories depending on the position in which the sensor resistance is connected.

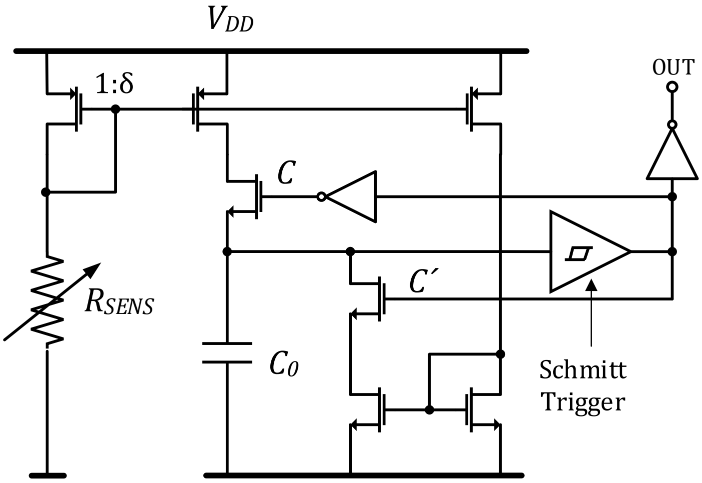

Figure 1.7: Oscillator-based readout with MOX sensor isolated from the oscillating circuit (adapted from [33])

In the simple architecture reported in Figure 1.6, the sensing element R_{SENS} is placed inside the oscillating circuit. This creates additional problems due to the unavoidable parasitic capacitance of the sensor, which affects the oscillation frequency since large voltage swing are applied on the sensor terminals. Although it is possible to compensate the parasitic capacitance effect [28], this problem can be avoided entirely isolating the sensing element from the oscillating part of the circuit, as proposed in [29] [30] and [33]. An example of an oscillator architecture with separated R_{SENS} is reported in Figure 1.7. The idea is to use the resistance to generate a current proportional to the resistance itself, and then using the generated current to charge and discharge a capacitance.

Another popular solution, typically used to extend DR and/or reduce measurement time, consists in combining the time domain approach with some sort of programmability, but this also increases complexity, costs and consumption, similarly to multi-scale voltage-readout approaches. In [31] a moving threshold oscillator is presented, a solution that allows a much faster measurement time but achieves poor linearity (5 %) due to the high complexity. Also in [29] different operative modes are used to increase dynamic range (by linking different scales) or to reduce measurement time, increasing complexity.

1.4 Thesis Objectives

The aim of this work is to develop CMOS readout interfaces able to satisfy modern requirements in the gas sensing industry for mobile applications. Given all MOX sensors interface requirements and typical problematic mentioned above, the final mandatory specification for the readout are summarized in the following list:

- Large resistance DR, at least 4-decades (resistance DR $\geq 80\,\text{dB}$)
- High accuracy and precision (relative error $< 0.5\,\%$, SNDR $> 46\,\text{dB}$)
- Fast output data rate ($> 1\,\text{Hz}$)
- Low power consumption ($< 1\,\text{mW}$)

Cheap implementation and design simplicity are also mandatory, thus complex, multi-scaling auto-ranging architectures are discarded. The chosen readout approaches are based on the time-domain Resistor-Controlled Oscillator similar to the solution proposed in [29], which places the sensor outside of the oscillating part of the circuit, ensuring better performances. Oscillator-based readouts are able to guarantee the large DR and precision requirements, however, reaching desired output data rate can be difficult. The goal is to solve the typical measurement time slowness of such approaches with aggressive design strategies and system-level optimization, boosting the oscillation frequencies to achieve fast output data rates, maintaining minimal power consumption. A relatively scaled CMOS technology node (a standard 130 nm process provided by Infineon), compared to the typical implementations in this field, has been chosen, to increase speed and reduce power, even if this can introduce several additional design challenges to achieve target performances. Moreover, to guarantee low-cost and simplicity, resistance readout and following digital conversion must be achieved using a single measurement scale and simple integrated digital logic. External micro-controllers and/or complex and power hungry architectures must be avoided.

Additionally, since a complete gas sensing micro-system requires multiple information from different sensors to improve pattern recognition algorithms and gas discrimination capabilities, this thesis will also address two critical points:

- Multiplexing support

- Compatibility with capacitive sensors

The ASIC must be able to multiplex between a matrix of different MOX sensors without decreasing readout performances. It is also very important to develop support for capacitive sensors readout, allowing easy connection of humidity sensors, which are based on capacitance variations. This could significantly improve the whole system performances, since humidity presence strongly affects MOX sensors behavior.

This work aims to develop a Matlab-Simulink model to optimize oscillator-based architectures and then to realize several silicon prototypes able to satisfy all requirements and specifications mentioned above. In particular, the focus of the first test-chip will be developing the core of the oscillator, ensuring that requirements of dynamic range, precision, speed and power consumption are met. In the successive test-chips, then, the focus will be on improving the architecture to ensure that multiple sensors can be connected, including the possibility to use capacitive sensors with the same core oscillator readout architecture.

Chapter 2

Modelling of Oscillator-Based Readouts

Proof of concept and system level optimization of the oscillator-based readout architectures are performed developing a Matlab-Simulink model. This chapter starts describing the basic principle behind the resistance-to-frequency conversion and the non-idealities of the CMOS implementation. Then, system specifications and design constrains for the main CMOS building blocks are derived from the model, ensuring that all specifications mentioned in section 1.4 are met. All readout architectures chosen for this work are based on the same time-domain Resistor-Controlled Oscillator core with the sensing element outside of the oscillating circuit, and are optimized with this model.

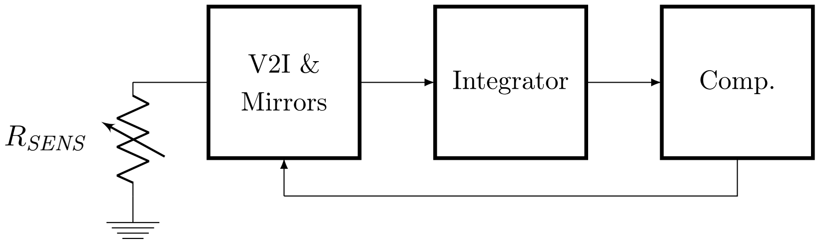

Figure 2.1: General oscillator architecture block diagram

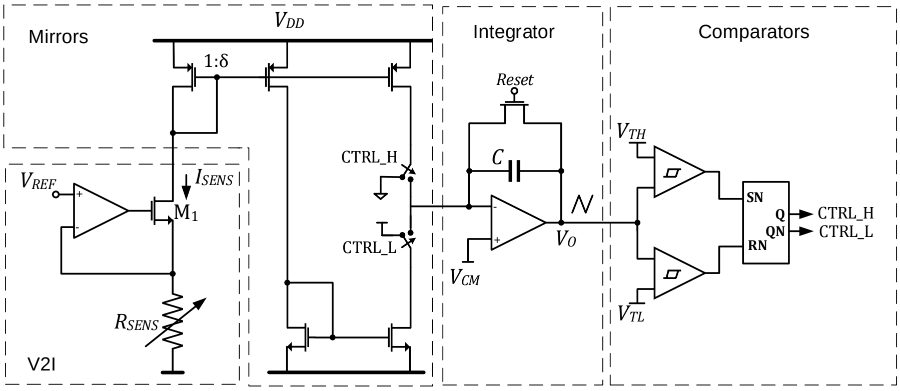

Figure 2.2: CMOS implementation of Resistance-to-Period architecture

2.1 Ideal Behavior

2.1.1 Resistance-to-Time

The basic building blocks of the oscillator architecture to perform the resistance to time conversion are shown in Figure 2.1, while a possible CMOS implementation of this readout is reported in Figure 2.2. Obviously there might be slightly variations in the CMOS implementations depending on target specifications and/or sensor requirements and each block can be realized in numerous ways. Nevertheless each architecture implemented in this work is composed by the key building blocks of Figure 2.1 which are:

- a Voltage-to-Current (V2I) converter
- a series of current mirrors
- an integrator block
- a comparator block

The V2I converter provides a constant voltage biasing V_{REF} on R_{SENS}, while the current mirrors are used to fed the sensor current I_{SENS} to the integrator block. The integrator performs the current-to-time conversion exploiting the well defined time behavior of a constant current charging and discharging a known capacitance C (Equation 2.1).

$$V_O(t) = \frac{I_{SENS}}{C} \int_0^t dt' \tag{2.1}$$

If the current I_{SENS} is constant during the integration time, the output voltage of the integrator V_O will rise or fall linearly over time depending on the sign of the current itself. The comparator block is then used to detect when V_O reaches a high(low) threshold and alternately inverting the I_{SENS} sign, keeping the integrator output bounded in a precise voltage window, with a period proportional to the sensor resistance R_{SENS}.

Considering the CMOS implementation reported in Figure 2.2, the oscillation period of the triangular waveform V_O is then:

$$T_{OSC} = \frac{2C \cdot \Delta V}{\delta \cdot V_{REF}} \cdot R_{SENS} = \alpha \cdot R_{SENS} \tag{2.2}$$

where $\Delta V = V_{TH} - V_{TL}$ is comparators switching window and δ is the current mirroring ratio. In this ideal scenario T_{OSC} is directly proportional to the sensing element value with a proportionality constant $\alpha = \frac{2C \cdot \Delta V}{\delta \cdot V_{REF}}$.

2.1.2 Time-to-Digital

The conversion of the oscillation period T_{OSC} in the digital domain is simply performed by counting how many oscillations occur in a precisely defined time window. At the beginning of each measurement, a reference clock is used to drive one counter, while the signal with the T_{OSC} information drives a second counter. The measurement ends when the counter driven by the reference clock reaches a defined value N_{REF}, and the measured data is represented by the value N_{OSC} reached by the second counter driven by the sensor signal.

Depending on DR and minimum digital resolution requirements is it possible to determine the number of bits necessary for the sensor counter and the duration of the time window (Δt). The minimum number of bits is obtained from Equation 2.3

$$N_{bit} \geq \log_2 \left(\frac{R_{max}}{R_{min}} \right) + N_{res} \tag{2.3}$$

where R_{max} and R_{min} are respectively maximum and minimum R_{SENS} values and N_{res} is the number of bit allocated for the minimum resolution, while the measurement time depends on how much time is necessary for N_{OSC} to reach the minimum value $2^{N_{res}}$ set by the resolution requirement in the slowest oscillation

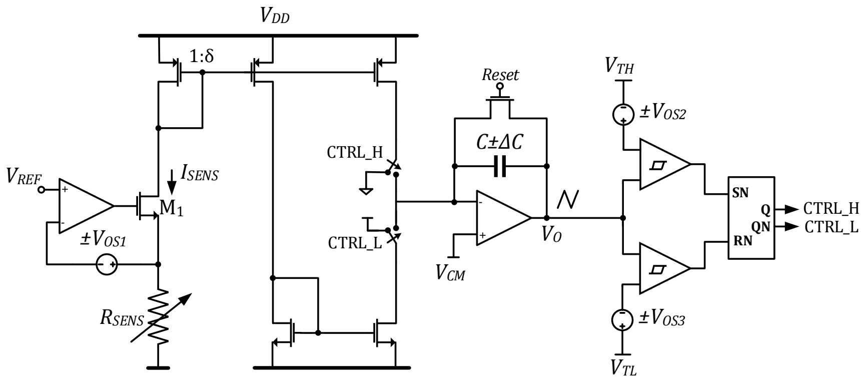

Figure 2.3: Resistance-to-Period architecture with offsets and ΔC

condition (when R_{SENS}=R_{max}).

$$\Delta t = T_{OSC}\big|_{max} \cdot 2^{N_{res}} = \alpha \cdot R_{max} \cdot 2^{N_{res}} \tag{2.4}$$

Wide DR with good measurement resolution can be achieved by using long time windows and/or small α values, at the cost of long measurement times and/or fast (and power hungry) oscillation frequencies.

2.2 Non-Ideal Behavior

Equation 2.2 does not take into account errors and non ideal behaviors introduced by the CMOS implementation of the architecture. Indeed different types of error can affect the measurement but they can be divided in two main categories:

- calibrable errors
- non-calibrable errors

2.2.1 Calibrable Errors

This category includes all errors that can be considered static, i.e. that do not change during the measurement time and over the product life-cycle. They are caused by technological spread and mismatch of CMOS production process and cause static offsets in comparators and opamps and drift of passive components nominal values. Figure 2.3 shows the resistance to period architecture including

V2I opamp offset (V_{OS1}), comparators offsets (V_{OS2} and V_{OS3}) and ΔC variation. Although static offests can be minimized with layout techniques and/or active cancellations, the spread of MIM (Metal-Insulator-Metal) capacitors in modern CMOS process can be as high as 30%. The oscillation period considering these errors is then modified according to the following equation:

$$T_{OSC} = \frac{2(C \pm \Delta C) \cdot (\Delta V \pm V_{OS2} \pm V_{OS3})}{\delta \cdot (V_{REF} \pm V_{OS1})} \cdot R_{SENS} \approx (\alpha \pm \Delta\alpha) \cdot R_{SENS} \quad (2.5)$$

These errors do not affect the architecture linearity since they only impact the parameter α which is modified by a certain amount $\Delta\alpha$. In most gas sensing scenarios usually is not important the actual value of the sensing resistance, but only its relative variation in respect with a baseline in clean air, and a linear relation between R_{SENS} and T_{OSC} is sufficient to extract the gas information. Nevertheless if the exact absolute value of resistance need to be measured, the accurate value of α can be determined with a simple calibration process using a known resistance after chip fabrication.

2.2.2 Non-Calibrable Errors

The calibration process can be used to eliminate static offsets but, unfortunately, offset errors can also be strongly dependent on voltage and temperature variations and $\Delta\alpha$ could change during measurement and/or between different measurements, causing a linearity error in the estimation of R_{SENS} that can compromise correct gas detection. Offset drift due to temperature variations can indeed become particularly critical since very high temperatures are necessary to correctly operate the sensor. It is important then to better estimate offsets impact in the measurement to avoid linearity error in R_{SENS} detection. Always referring to the circuit in Figure 2.3 and starting considering only V2I offset V_{OS1} contribution, Equation 2.5 can be rewritten as:

$$T_{OSC} = \frac{2C \cdot \Delta V}{\delta \cdot V_{REF}} \cdot R_{SENS} \left(\frac{1}{1 \pm \frac{V_{OS1}}{V_{REF}}} \right) \quad (2.6)$$

and the obvious conclusion is that V2I offset error is minimized when $V_{REF} \gg V_{OS1}$. With similar considerations is it also possible to conclude that comparators offset errors become negligible when $\Delta V \gg V_{OS2} + V_{OS3}$. Moreover, if comparators are matched ($V_{OS2} \simeq V_{OS3}$), both threshold voltages V_{TH} and V_{TL} will be translated by the same amount, leaving almost constant the switching window ΔV, and further reducing comparators offsets impact.

The parameter δ can also cause some linearity errors. Current mirroring ratio precision depends on the robustness of transistor level implementation of mirrors and in this application can be challenging to obtain very high mirroring accuracy. Indeed, since R_{SENS} variation is very large, current mirrors must be able to process a wide range of currents and current mirroring ratio can vary from the nominal value δ especially when approaching the extremes of R_{SENS} range to cover. This effect is also strongly affected by PVT that can increase the non linear behavior of current mirrors.

Another non-ideal behavior is due to delays. The voltage output V_O is ideally bounded between the two threshold voltages by inverting the current sign when one of the two threshold level is reached, but in reality there is a delay between threshold detection and actual sign inversion. This delay causes the integrator output to go beyond the threshold voltages until the feedback network actually perform the current sign inversion, and the oscillation output is then:

$$T_{OSC} = \frac{2C \cdot \Delta V}{\delta \cdot V_{REF}} \cdot R_{SENS} + t_d \tag{2.7}$$

where T_{OSC} is increased by a certain delay t_d that causes a non-linear relationship between R_{SENS} and T_{OSC}. The main source of delay in the feedback action is comparators response time which should be as fast as possible to minimize t_d. It is quite obvious that all delay related effects become more and more critical the faster is the oscillation frequency. Another problem that arises during fast oscillations is that the voltage output of the integrator $V_O(t)$ no longer depends only on C and I_{SENS} values (Equation 2.1), but second order effects due to the limited bandwidth of the opamp used in the integrator block causes some distortions in the $V_O(t)$ signal, compromising linearity.

In conclusion, calibrable errors include integrator capacitor variations and static offsets due to technology process spread, while non-calibrable errors include variable offsets, non-linear-mirroring ratio and delay related problems.

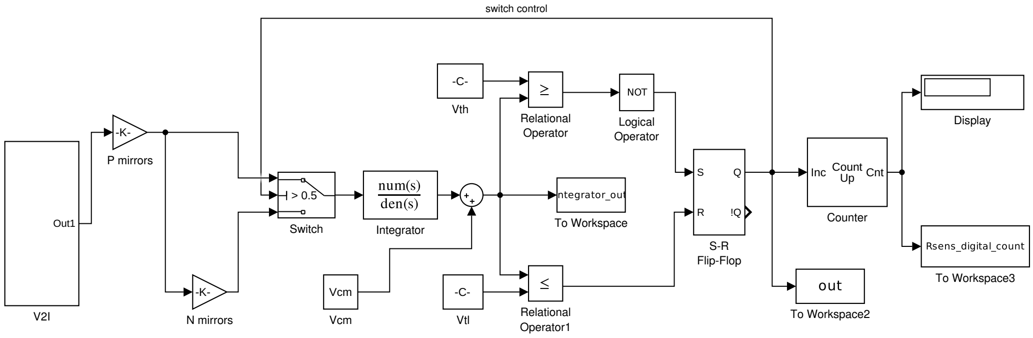

Figure 2.4: Simulink Top Level

2.3 Matlab-Simulink Model

The Matlab-Simulink model used for system level optimization uses combinations of the ideal and non-ideal equations described in the previous sections, Matlab scripts and functions, and Simulink blocks from the standard and *Simscape* libraries. The top-level view of the Simulink is shown in Figure 2.4, which includes all blocks necessary to implement the resistance to digital conversion (V2I, integrators, ...). More details on each block implementation and functionality will be addressed later in this section while showing some significant simulation results useful for architecture optimization.

Table 2.1 defines the target specifications for the first test-chip: sensor resistance range, resolution, measurement time Δt and maximum sensor current; specs that satisfy the general requirements for gas sensing applications discussed in chapter 1. Power consumption for the readout should be as low as possible and the maximum current in the target sensor should not exceed 500 µA. The $I_{SENS}|_{max}$ limitation leads to a sensor biasing voltage of

$$V_{REF} = 500\,\mu\text{A} \cdot 100\,\Omega = 50\,\text{mV} \tag{2.8}$$

Table 2.1: First test-chip specifications

R_{SENS}	$100\,\Omega$ - $1\,\text{M}\Omega$
$I_{SENS}\|_{max}$	$\leq 500\,\mu\text{A}$
Resolution (N_{res})	0.4% (8-bits)
Measurement Time (Δt)	250 ms

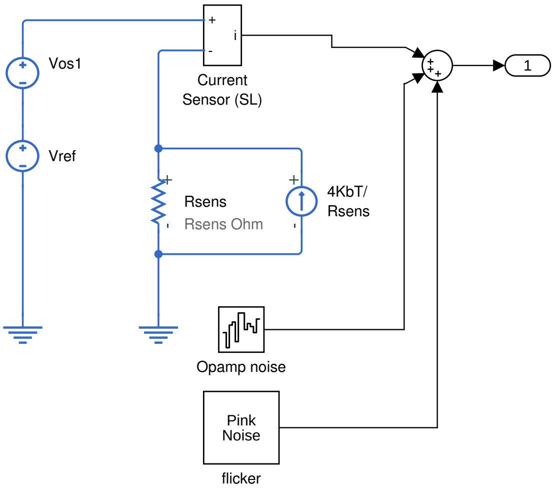

Figure 2.5: Simulink V2I converter block

while considering design Equations 2.2 and 2.4 the other specifications are met choosing the correct value for the parameter $\alpha = \frac{2C \cdot \Delta V}{\delta \cdot V_{REF}} = 976.56\,\text{ps}\,\Omega^{-1}$.

As discussed before, voltage reference and comparatos switching windows should be as high as possible to limit offest impact, but in this case, V_{REF} is fixed by sensor biasing requirements (Equation 2.8) to only $50\,\text{mV}$ and ΔV is obviously limited by integrator voltage output swing, which is limited by the power supply and circuit topology. ΔV is set at $800\,\text{mV}$, which is the maximum reasonable value obtainable considering CMOS technology used and chosen architecture. The other parameters are mirroring ratio $\delta = 1/10$ and integrator capacitance $C = 3.05\,\text{pF}$. More details on transistor level implementations and parameters value can be found in the next chapters.

2.3.1 Offsets Impact

To better estimate V2I offset impact considering the low value of V_{REF}, a series of simulations are performed. In Figure 2.5 the V2I block of the Simulink is shown. The sensor resistance is biased with the constant V_{REF}, while the offset V_{OS1} is generated using the Matlab normally distributed random numbers function with different reasonable value of standard deviations. In these simulations noise generators are switched off and also all others Simulink blocks are set with the ideal behavior to highlight only V2I offset impact.

Figure 2.6 shows digital output code uncertainty for different vales of V2I

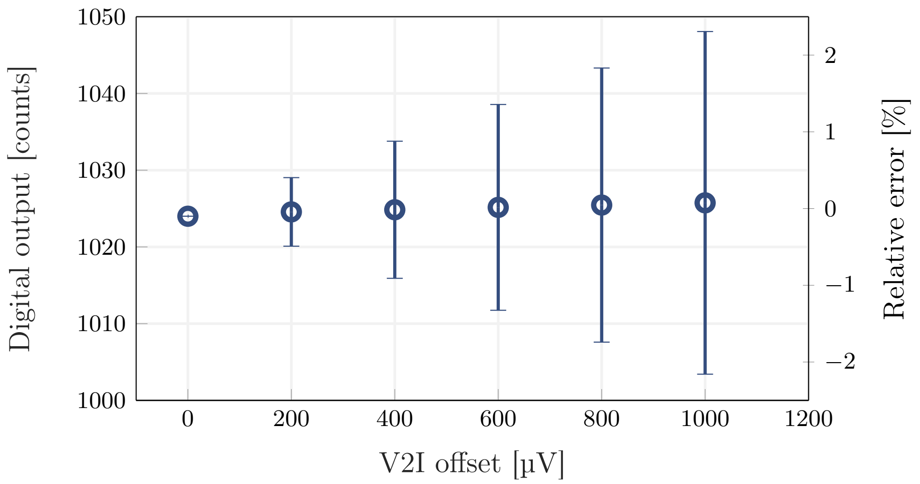

Figure 2.6: V2I offset impact

offset. It can be clearly observed that the relative error compared with the ideal digital code ('1024' in this case) exceed the target specification (0.4%) with few hundreds of µV of V2I offset. Although this error can be compensated if constant during chip life-cycle as discussed in section 2.2, V2I offset must be lower than 200 µV during PVT variations. Similar simulations show that comparators offset has a much lower impact on the final measurement because of the much larger value of voltage ΔV, as expected.

2.3.2 Delays Impact

The parameter α has been set to $976.56\,\mathrm{ps}\,\Omega^{-1}$ to satisfy target specifications and, considering the worst case sensor resistance value of $100\,\Omega$, the fastest interface oscillation has a period of only $T_{OSC}|_{min} = 97.65\,\mathrm{ns}$. Since it is mandatory to achieve low power consumption, the Simulink model has been used to detect minimum requirements for the integrator opamp and comparators, in order to avoid over-design of these power hungry components. Indeed power consumption increase drastically for higher oscillation frequencies because the circuit must be able to follow the signal without introducing significant delays and distortions and in CMOS implementations speed is always related to power consumption.

The integrator in the Simulink circuit is modeled with a transfer function block and the integrating opamp is approximated as a first-order (one pole) system with a certain DC Gain and unity-gain-bandwidth (UGBW). By sweeping DC

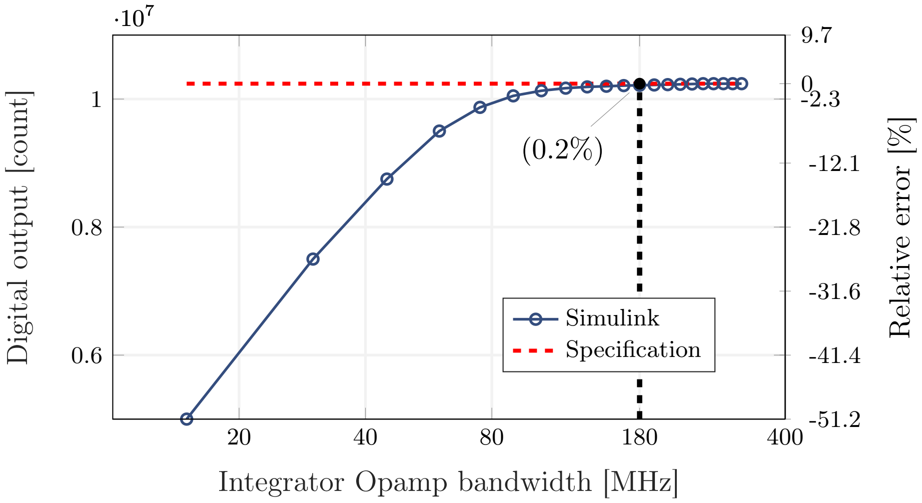

Figure 2.7: Integrator Opamp bandwidth impact

gain and UGBW values in worst-case conditions it is possible to determine the minimum requirements for the opamp. As expected a low UGBW is the opamp most significant limiting factor. In Figure 2.7 the digital output code in fastest oscillation condition (10.24 MHz) is plotted against the integrator opamp UGBW and compared with the ideal digital output vale. The signal distortion increases for slow UGBW frequencies and when the bandwidth becomes slower than 180 MHz, the integrator distortion cause a linearity error higher than 0.2% which is no longer acceptable, thus setting design requirement of at least 180 MHz of bandwidth for the integrator.

With a similar approach the maximum delay of comparators is also determined, and the response time is set to be < 400 ps.

2.3.3 Noise

Up to this point noise performances were not discussed, and the reason is that the architecture is intrinsically very insensitive to noise. Indeed a major advantage of the time-domain approach is that white noise is averaged over the long measurement time thus not affecting the final R_{SENS} measured value. To prove this assumption, the major noise contributions are added to the Simulink model. In Figure 2.5, for example, the V2I block includes both thermal and flicker noise contributions from the sensor element and form the Opamp. The sensor thermal noise, which is the dominant source, is modeled as a noise current

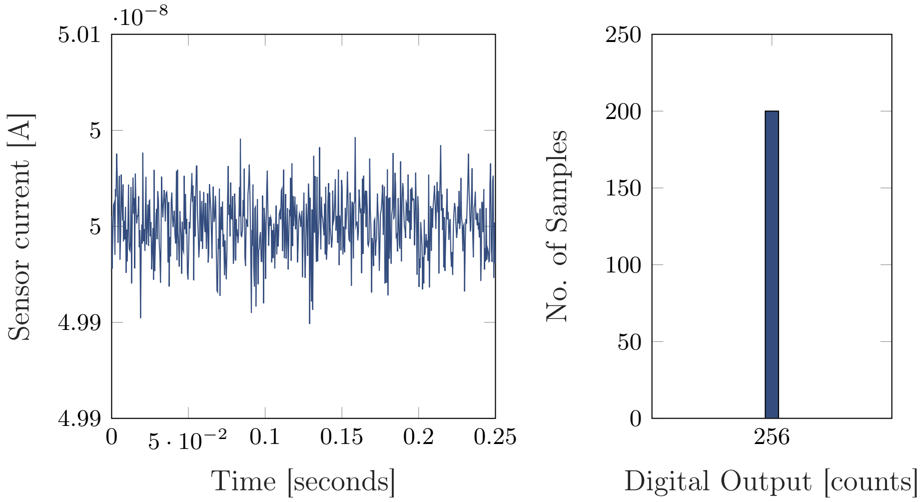

Figure 2.8: Sensor noise impact

generator in parallel with the sensing resistance having a power spectral density of:

$$S_I(f) = \frac{4k_BT}{R_{SENS}} \tag{2.9}$$

The root mean square value of the sensor noise current is:

$$i_n = \sqrt{\frac{4k_BT\Delta f}{R_{SENS}}} \tag{2.10}$$

and the signal to noise ratio (SNR) of the V2I converter can be easily calculated and is:

$$\text{SNR} = \frac{I_{SENS}}{i_n} = \frac{V_{REF}}{\sqrt{R_{SENS}}} \cdot \frac{1}{\sqrt{4k_BT\Delta f}} \tag{2.11}$$

Equation 2.11 shows that the SNR decreases for higher R_{SENS} values and in Figure 2.8 a simulation is reported highlighting the sensor noise current in worst-case conditions (R_{SENS}= 1 MΩ) and the corresponding digital output count which is always constant for 200 acquisitions. This confirms the intrinsic robustness of the architecture to white noise.

Also flicker noise does not affect the overall output count significantly: indeed in the time domain flicker noise behaves similar to thermal noise having a zero average but with higher peak values.

Chapter 3

UB01 Prototype: Single Channel R-to-T Converter

The first silicon prototype (UB01) of an oscillator-based readout interface has been designed and produced using a standard 130 nm CMOS technology provided by Infineon Technologies AG. This prototype is optimized for the target specifications reported in Table 2.1 and it is designed following the Simulink model results and top-level design equations of the previous chapter.

The technology chosen (130 nm @ 1.5 V) is one of the most aggressive implementation in terms of scaling in this field. In fact, scaling the technology introduces several design challenges to achieve the target performances, mostly due to the limited power supply and dynamic range and worst linearity performances of scaled devices. Nevertheless the choice allows to reduce overall power consumption and boost the oscillator frequencies to meet time measurement specifications. Moreover, scaling down is particularly advantageous since the sensor interface has to be realized embedded in complex mixed-signal SoC products, where large digital sections are exploited for pattern recognition. The total current consumption of UB01 front-end is 450 µA and more details on the architecture and on each CMOS block implementation will be addressed in the next sections.

3.1 ASIC Implementation Details

UB01 architecture is reported in Figure 3.1 The V2I converter is composed by Opamp A_1 and transistor M_1. It provides the biasing voltage on the positive

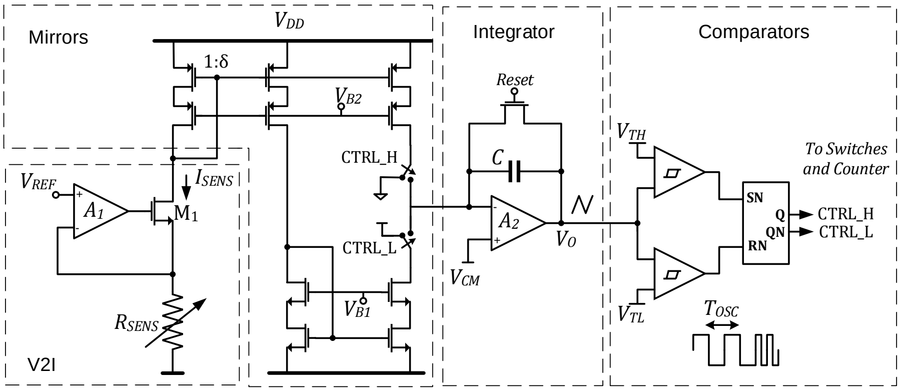

Figure 3.1: UB01 architecture: single-channel, grounded R_{SENS}, R-to-T converter with digital output

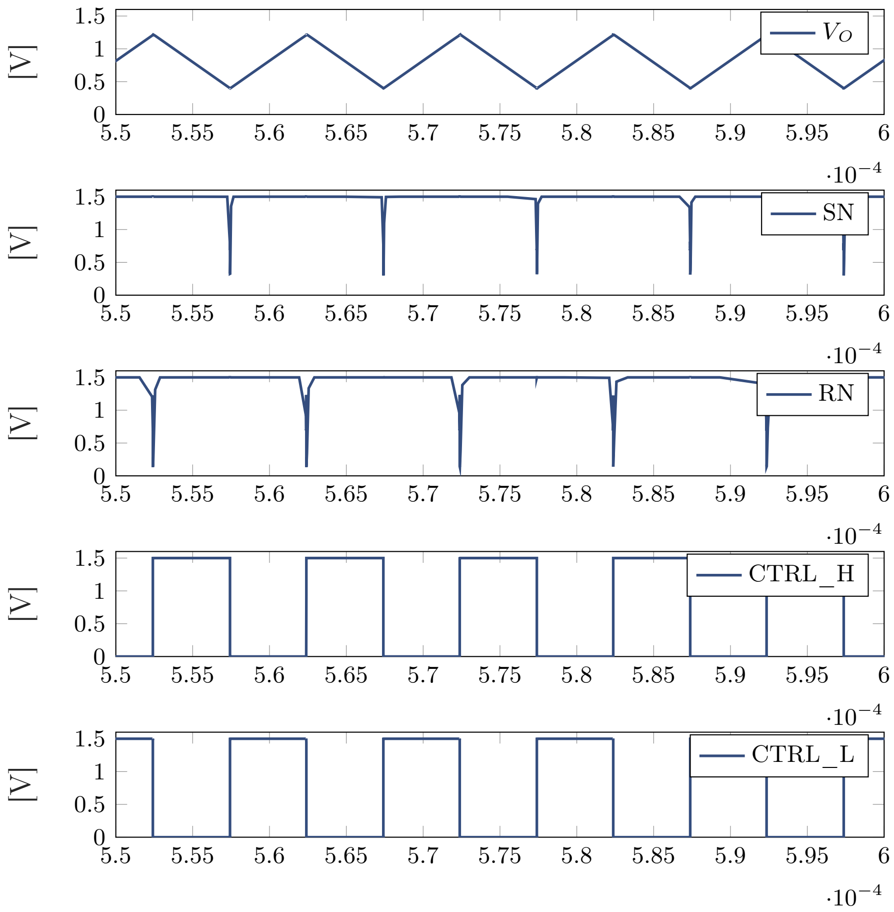

Figure 3.2: ASIC timing diagram

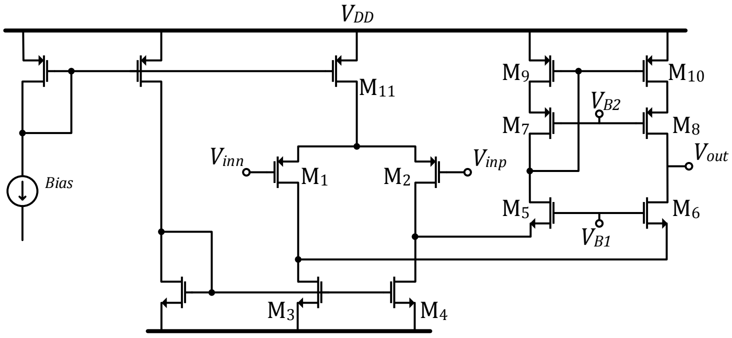

Figure 3.3: V2I Opamp. DCgain = 94 dB, I = 5 µA, φ_m = 80°

terminal of the sensing resistance R_{SENS} using a stable reference and bias voltages V_{REF} generated by an internal bandgap circuit, while the other sensor terminal is connected to ground. The sensing current I_{SENS} is then mirrored and alternatively sunk from or sourced in the virtual ground of integrator Opamp A_2, according to control signals CTRL_H and CTRL_L. The integrator output voltage V_O is a triangular waveform that is compared to the two reference voltages V_{TH} and V_{TL} generating switches control signals and steering the current. An additional flip-flop always guarantees that comparators synchronously switch. In Figure 3.2 a simulation shows the ASIC timing diagram while converting 100 kΩ of sensor resistance. The triangular shape of the integrator output V_O can be observed, as well as comparators threshold detection signals (SN, RN) and switches control signals.

3.1.1 V2I Converter

The sensing resistance is biased with a low-offset, high gain folded cascode p-mos input pair Opamp (schematic in Figure 3.3) and a nmos source follower M_1. Biasing accuracy is critical since the applied reference voltage V_{REF} is only 50 mV to avoid large current consumption on the sensor when the resistance becomes small. In order to guarantee that V_{REF} is precisely applied to R_{SENS} the V2I converter must ensure very low output resistance at the buffered V_{REF} node to avoid significant voltage drop when sensing high currents. The low output impedance is guaranteed by the presence of source follower stage M_1 and by the feedback structure in combination with the very high Opamp gain (94 dB). This

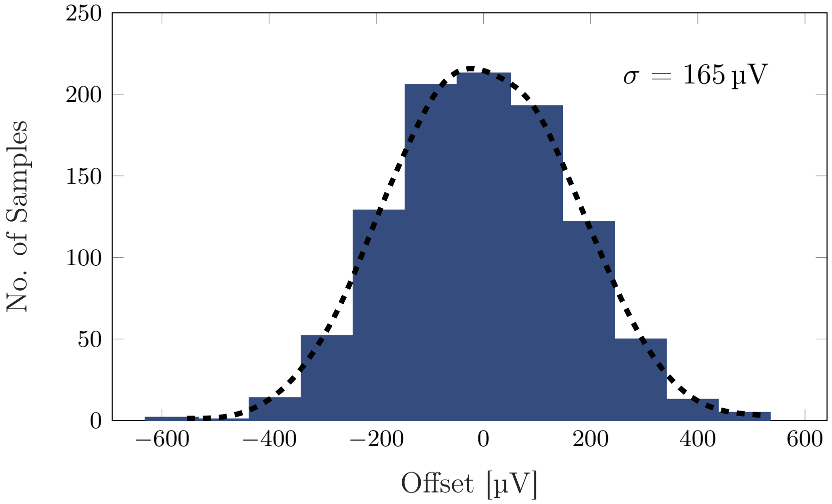

Figure 3.4: V2I Opamp offset. Montecarlo process & mismatch simulations

guarantee a linearity error better than 0.1% in the voltage-to-current conversion even when $I_{SENS}|_{max} = 500\,\mu A$.

Target low offset specs are achieved without using complex and power hungry solutions to dynamically remove offset, like chopping or auto-zero, but simply exploiting large input stage transistors M_1 and M_2 (W=300 µm, L=10 µm) and interdigitated layout techniques. Offset during PVT variations is always lower than few tens of micro volts (offset temperature coefficient drift $\approx 0.1\,\mu V\,{}^\circ C^{-1}$), while the Opamp performs only 165 µV of offset (1σ) in Montecarlo process and mismatch simulations as highlighted in Figure 3.4, thus satisfying the strong offset requirements defined in subsection 2.3.1.

The Opamp operates in sub-threshold region consuming only 5 µA of current.

3.1.2 Current Mirrors

The low-voltage folded-cascode current mirrors that connect V2I to the integrator Opamp are designed to guarantee the desired linearity and resolution in all the current sensor dynamic range (500 µA - 50 nA), They operates in push-pull configuration where the sensor current is steered by two transmission gate switches controlled by the digital logic (signals CTRL_H and CTRL_L). To further reduce power consumption and to fulfill system requirements on integrator and comparators, a mirroring ratio δ, 1:10, is used meaning that the smallest integrated sensor current is only 5 nA when sensing $R_{SENS}|_{max} = 1\,M\Omega$.

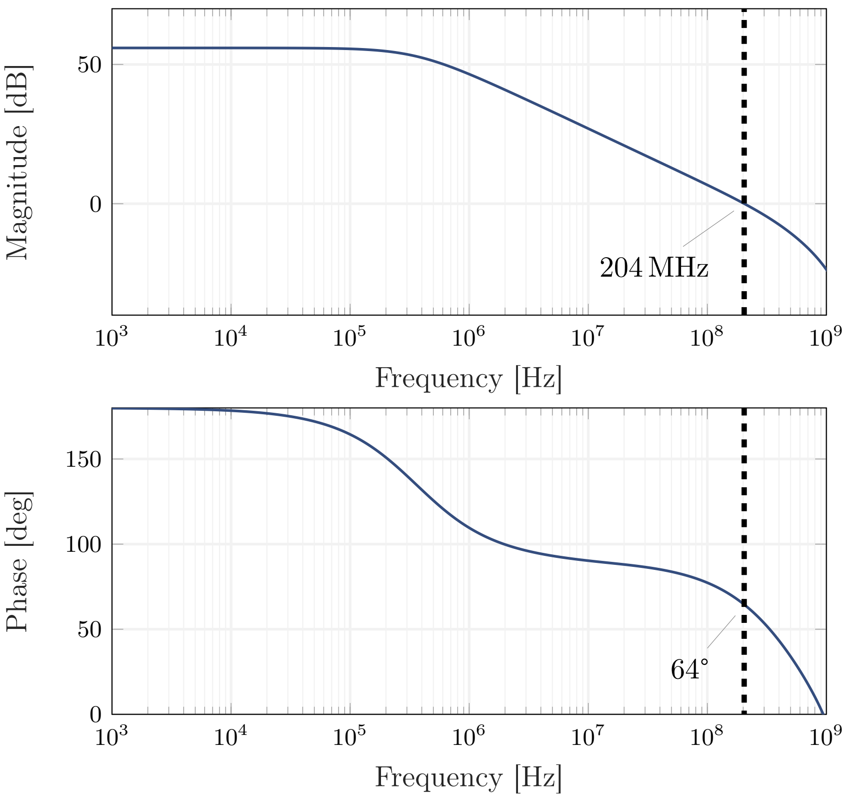

Figure 3.5: Integrator Opamp frequency response

The lower limit in the mirrored sensor current is fixed by leakage currents and mirroring errors which are no longer negligible for smaller currents causing the linearity to rapidly decreases. This error is particularly evident in the nmos mirror branch since two mirroring operations are required to generate the current.

3.1.3 Integrator

The most important integrator Opamp design constraint is high bandwidth to cope with the fast oscillations of the R-to-T converter. A telescopic single stage topology then, seems the best fit to maximize power/bandwidth efficiency but it has the drawback of very limited voltage output swing, especially at 1.5 V of power supply. The best design solution is achieved using a n-input single-stage folded-cascode Opamp able to perform 55 dB of DC-gain, 200 MHz of bandwidth and capable of 0.8 V of output swing while charging and discharging an integrator capacitance of 3 pF. The Opamp frequency response is plotted in Figure 3.5. The total current consumed is 250 µA.

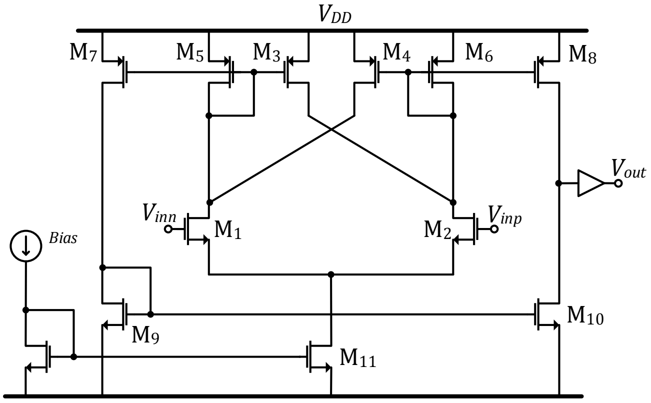

Figure 3.6: Continuous time comparator

3.1.4 Comparators & Logic

The two comparators (schematic in Figure 3.6) that control current steering switches and effectively bound the integrator output voltage have to operate in continuous-time way and are optimized for fast response time ($< 400\,\text{ps}$) with an average current consumption of only $80\,\mu\text{A}$ each. The upper threshold voltage V_{TH} is $1.2\,\text{V}$ while the lower V_{TL} is $0.4\,\text{V}$. Large output voltage swing $\Delta V = 0.8\,\text{V}$ and good matching between the two comparators provide great robustness to offset errors. Indeed matched comparators offset translate both V_{TH} and V_{TL} of the same amount, not affecting the oscillation period. Metastability issues are solved by the presence of the SR asynchronous latch which forces each comparator to switch alternately. Sensor and reference counters, control logic and serial data output blocks are implemented with the synthesis of VHDL code[1]. The ASIC includes also an internal reference clock running at 500 kHz.

3.2 Electrical Characterization

3.2.1 Experimental Setup

The developed ASIC includes most of the additional blocks needed for proper front-end functioning, (bandgap, voltage references and regulators, internal reference oscillator, additional digital logic, ESD protections,..) thus only requiring

---

[1] more details on control logic implementation and VHDL code are presented in Appendix A

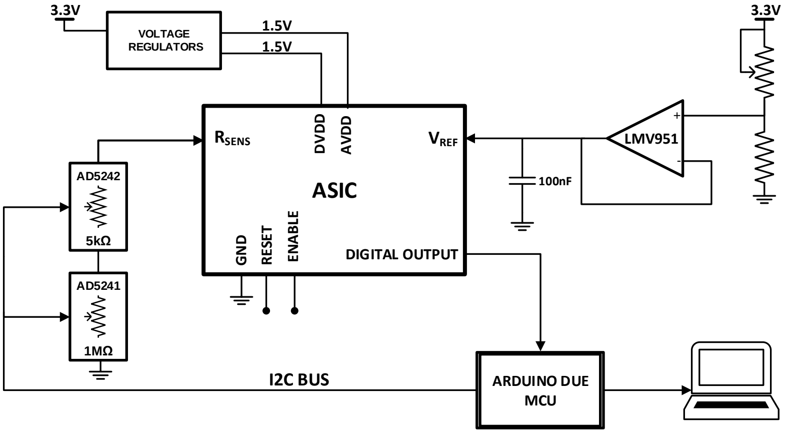

Figure 3.7: Simplified schematic of the electrical measurement setup

power supply, input sensor resistance R_{SENS}, V_{REF}, and output data acquisition for interface characterization. The ASIC allows also the connection of external clock and reference voltages for testing purposes. The custom PCB test board fabricated provides all needed supplies and voltages as well as connections with the data acquisition board, implemented with an Arduino DUE microcontroller. Since great precision on applying the voltage V_{REF} is required for precise characterization, instead of using a commercial regulator, V_{REF} is generated with a custom designed voltage reference circuit exploiting a high performance Opamp (LMV951) in buffer configuration (Figure 3.7). The Arduino DUE microcontroller is programmed to acquire digital serial data outputs of the logic and to control its enable and reset signals. All acquired digital data are stored on a PC for final elaboration.

The electrical characterization consists in evaluate the performances of the ASIC in term of resolution, noise, linearity and DR. To obtain consistent measurements it is important to correctly emulate the sensor resistance R_{SENS} covering the wide range of interest. Moreover the emulated R_{SENS} should be able to change its value relatively fast in order to reproduce the typical behavior of a MOX sensor. R_{SENS} is emulated using two 256-positions, digitally controlled variable resistor devices (AD5241 and AD5242) connected in series as shown in Figure 3.7. The two digital potentiometers (DigiPots) are then connected at the ASIC input sensor pin. The first potentiometer has a nominal resistance value of $1\,\mathrm{M\Omega}$ and is used to perform the coarse variations of R_{SENS}, while the second potentiometer of

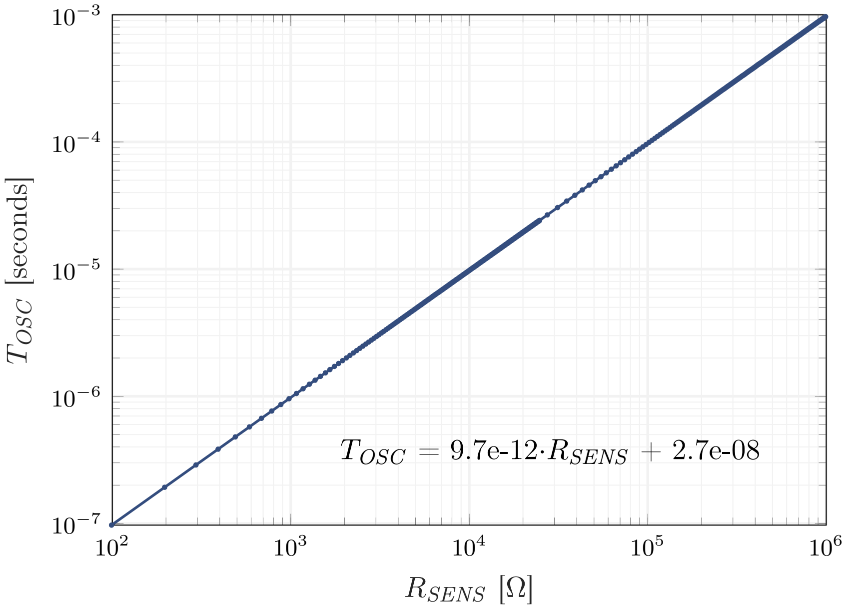

Figure 3.8: UB01 characterization: T_{OSC} vs. R_{SENS} with linear fitting

5 kΩ allows a much finer R_{SENS} adjustment. By programming the two DigiPots values via the I2C protocol is it possible to obtain more than 65000 linearly spaced values of R_{SENS} ranging from ≈ 60 Ω (wiper contact resistance) to ≈ 1 MΩ with an LSB of ≈ 20 Ω. Before ASIC characterization, the emulated R_{SENS} values are precisely measured with a high resolution multimeter and stored on a PC, setting the baseline necessary to confront ASIC measurements and evaluate performances.

3.2.2 ASIC Measurements Results

To perform the interface electrical characterization the sensor resistance is always stepped every 250 ms (interface output data rate) for the whole 4-decades single-scale resistance range (100 Ω - 1 MΩ). In Figure 3.8 the acquired digital output count is converted into the corresponding interface oscillation period and plotted against R_{SENS}, then a linear fit is applied to the data. The oscillator gain vale obtained from the fit (parameter α) is close to the theoretical one. Interface measured relative error and corresponding SNDR (Signal to Noise and Distortion Ratio) are then plotted in Figure 3.9 and Figure 3.10, showing that the ASIC exhibits a maximum relative error of ±0.4 %, and that the corresponding SNDR is always better than 48 dB over the 4-decades range. This leads to an overall DR of 128 dB.

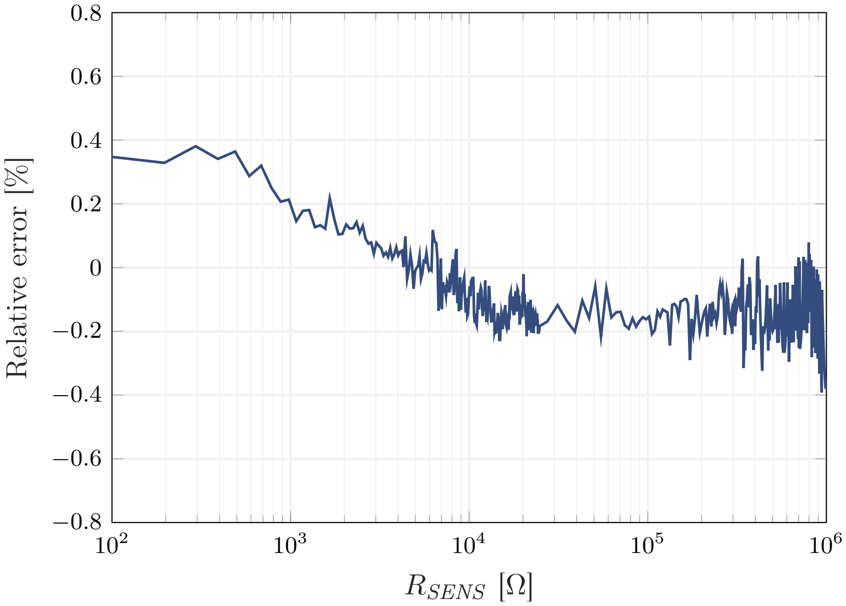

Figure 3.9: UB01 characterization: relative error vs. R_{SENS}

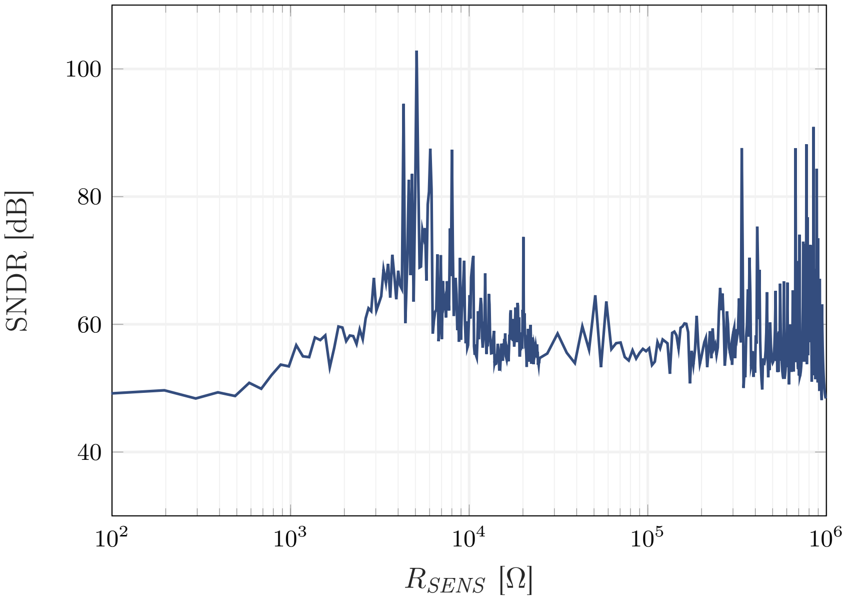

Figure 3.10: UB01 characterization: Signal to Noise and Distortion Ratio (SNDR) vs. R_{SENS}

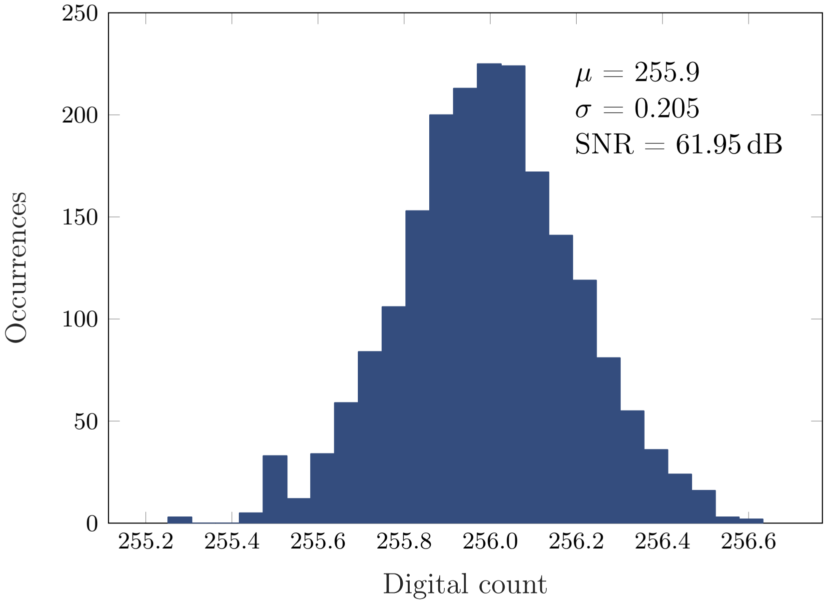

Figure 3.11: Noise persistence histogram plot with R_{SENS}=1 MΩ. 2000 acquisitions

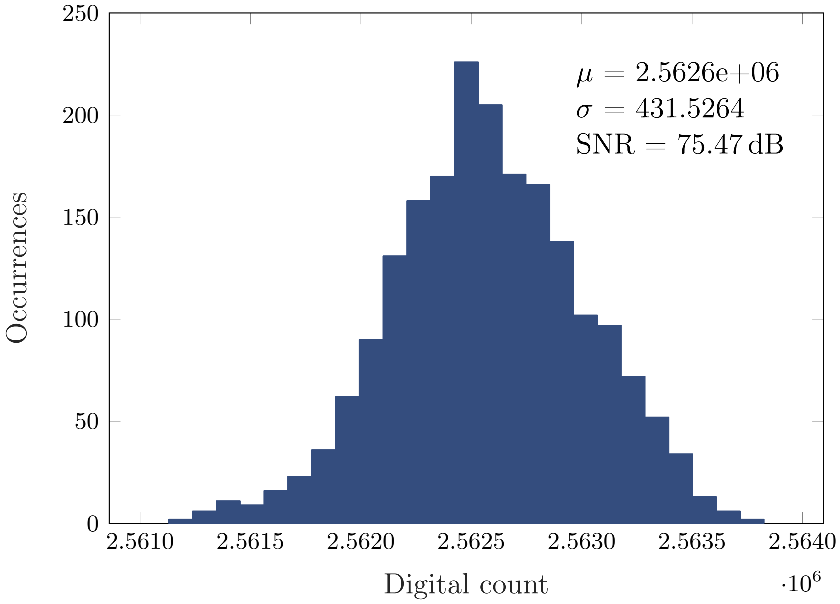

Figure 3.12: Noise persistence histogram plot with R_{SENS}=100 Ω. 2000 acquisitions

The relative error follows the expected trend: it starts close to the upper positive limit (0.4 %) when sensing small sensor resistances as the limiting factors are due to the fast oscillations, it gradually decrease to zero around R_{SENS} mid-scale and then increases again toward the negative limit (−0.4 %) as the sensor resistance increases. This behavior can also be observed in the SNDR plot, which shows a peak value at mid-scale and then the SNDR decreases toward the lower and upper limits of R_{SENS} range. Distortion effects dominate for low R_{SENS} values while noise effects can be observed when sensing higher R_{SENS}. Due to the nature of the ASIC digital conversion, the quantization error is not linearly distributed over the input sensor range but it decreases as the sensor resistance decreases (more digital counts and bits with higher oscillation frequencies). This effect in combination with V2I thermal noise, which is also a monotonically decreasing function of R_{SENS} (Equation 2.11), explains the observed behavior. The peak SNDR value at mid-scale is due to a precise design strategy in which the ASIC is specifically calibrated and optimized for mid-scale sensor resistance values, allowing optimal extension of the R_{SENS} range that can be converted with minimal distortion and max precision.

Also noise persistence measurements have been performed to underline interface noise sensitivity. The two histogram plots in Figure 3.11 and Figure 3.12 show noise persistence in the digital output when sensing maximum and minimum sensor resistance of $1\,\mathrm{M\Omega}$ and $100\,\Omega$ respectively. The histograms are obtained acquiring 2000 samples of the averaged interface oscillation frequency before the digital conversion and calculating the corresponding digital value. The SNR in worst-case scenario (when sensing $1\,\mathrm{M\Omega}$) is $\approx 62\,\mathrm{dB}$ and is dominated by sensor thermal noise, while at higher frequencies (lower sensor resistances) the SNR rises up to $\approx 75\,\mathrm{dB}$ which is the interface SNR limit @ 4 kHz of output data rate. Indeed the quite long measurement time, as expected, provides intrinsic robustness to noise since it is averaged and even in worst-case scenario the digital output variation due to noise is always better than the minimum 8-bit resolution of the digital quantization.

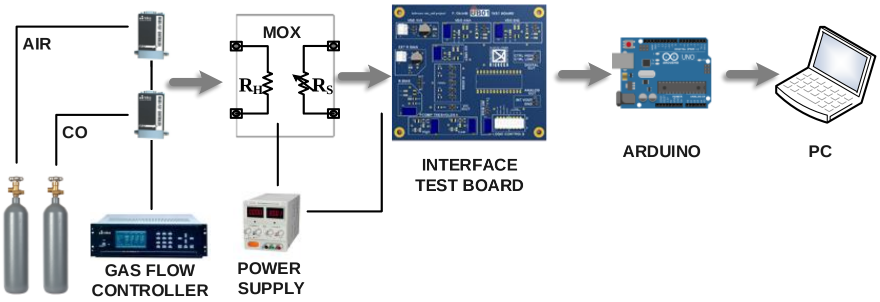

Figure 3.13: Chemical measurement setup

3.3 Chemical Characterization

3.3.1 Experimental Setup

The experimental setup used for actual chemical measurements is reported in Figure 3.13. All measurements have been performed in a controlled atmosphere at constant flow mode. The MOX sensor used is a custom-made micro-machined SnO_2 thin-film device which is placed in into a sealed test cell, connected with two distinct mass flow controllers (MFCs of MKS mod. 1179A). A multi-channel mass flow programmer (MKS mod. 647B) is then used to select the desired gas composition flowing into the chamber. The first gas channel is connected to air, which is used as reference gas, and the second channel to the gas under test (CO). All measurements have been performed maintaining a constant gas flow of 100 SCCM (Standard Cubic Centimeters per Minute) into the chamber and changing the CO concentration. The sensor has an embedded heater biased with an external power supply at constant power, to reach the operative temperature (350 °C to 400 °C), while the developed ASIC provides the biasing V_{REF} on the sensing layer. Again, the Arduino MCU is used for data acquisition of the resistance-to-digital data output.

3.3.2 ASIC Measurements Results

The first chemical test has been performed at a temperature of 400 °C, reached with a heating power of $\approx 50\,\mathrm{mW}$. Figure 3.14 shows the transient response obtained by exposing the sensor at different CO concentrations, from 25 ppm to

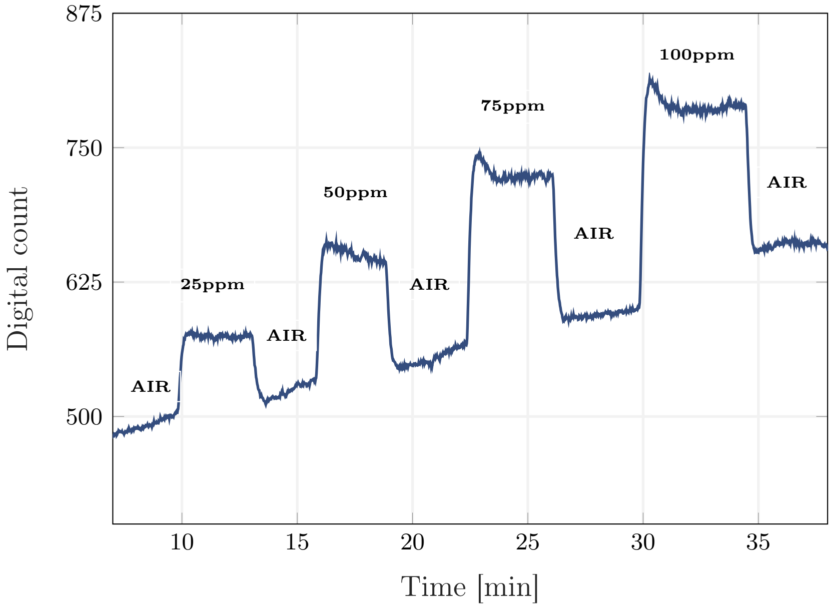

Figure 3.14: System response at different CO concentration alternated with air recovery at 400 °C. gas flow = 100 SCCM

100 ppm, with air recovery between each exposition. Is it important to remember that, since the target analyte to be detected is a reducing gas, the expected conductance variation should be positive, leading to faster oscillations (higher digital counts) when the CO concentration increases. Fast response and recovery time can be observed in the transient plot, but also a positive baseline drift, caused by a non-optimal operative temperature used to heat the MOX sensor. This shows the importance of setting and maintaining a correct operative temperature to ensure optimal results. Moreover, the adopted sensor was fairly new (less than 48 h of life) and some additional time was needed to reach its stable state. After a couple of days and different cycles of heating and cooling, the optimal working temperature has been determined to be around 350 °C (44 mW of open loop DC power), and a second set of measurements are plotted in Figure 3.15 and Figure 3.16. The sensor exhibits a better CO sensitivity thanks to a more conductive and stable baseline (digital count $\approx$ 1 800 or about 7.25 kHz of oscillation frequency) and with this set-up, the sensor and the interface were able to detect 5 ppm of CO with or without air recovery. The developed ASIC was able to correctly reads the sensor resistance even if the adopted MOX thin film exhibits a not very remarkable conductivity variation due to the CO presence.

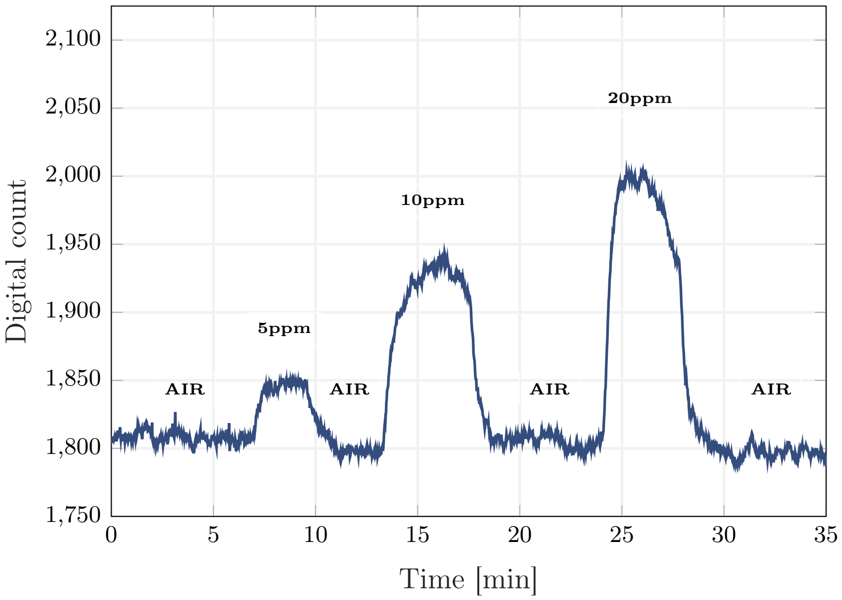

Figure 3.15: System response at different CO concentration alternated with air recovery at 350 °C. gas flow = 100 SCCM

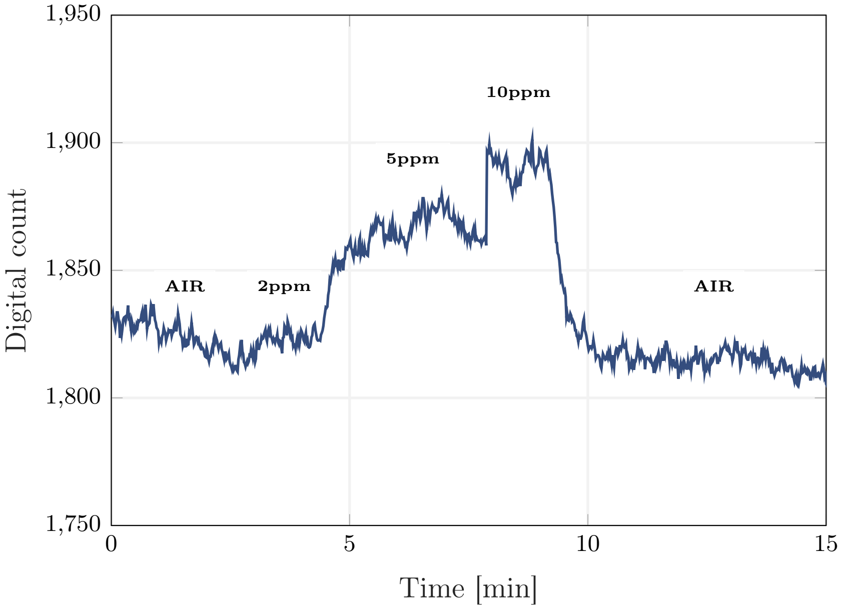

Figure 3.16: System response at different CO concentration without air recovery at 350 °C. gas flow = 100 SCCM

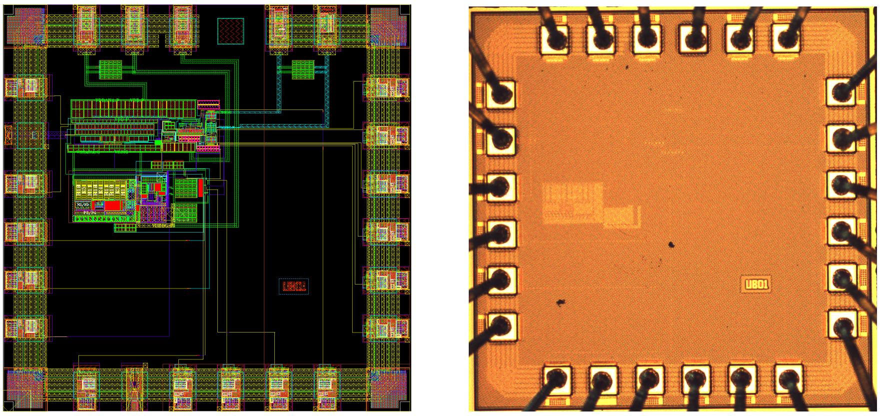
(a) Layout **(b)** Chip photo

Figure 3.17: UB01 test-chip

3.4 Conclusions

Table 3.1: UB01 performance resume

R_{SENS} range	100 Ω - 1 MΩ
Max relative error	±0.4 %
Worst-case SNDR	48 dB
Dynamic Range (DR)	128 dB
Min digital output equivalent precision	8-bits
Output data rate	4 Hz
Front-end power consumption	675 µW@1.5 V
Max sensor current	500 µA
Technology	130 nm CMOS
Core size	0.125 mm^2
Min CO concentration detected	5 ppm

This chapter summarizes details on transistor level architecture and most relevant measurement results of the first silicon prototype developed in this work. The oscillator-based UB01 test-chip architecture provides a versatile single-channel resistance-to-digital interface optimized for MOX sensors. Layout and a photograph of UB01 are shown in Figure 3.17, while Table 3.1 resumes the chip performances. The developed architecture provides 128 dB of dynamic range with a maximum measured relative error of $\pm 0.4\,\%$ (worst-case SNDR $\geq 48\,$dB) at a constant digital output data rate of 4 Hz, with a digital output composed by at least 8 significant bits. The interface is implemented in a standard CMOS 130 130 nm technology with an area of $0.125\,\mathrm{mm}^2$ while the total front-end power consumption is 675 µW @ 1.5 V. Electrical and chemical measurements with a real SnO_2 MOX sensor prove the validity of this front-end in a real gas sensing application. The sensor used in the chemical measurements shows a minimum CO detection capability in ambient air of 5 ppm, while the interface is able to correctly detect the sensor resistance variations.

The proposed ASIC is able to combine large dynamic range, small relative error, low power consumption and fast measurement time thus satisfying modern gas sensing requirements for mobile applications described in section 1.4.

Chapter 4

UB31-32-33 Prototypes: Multiplexing and C_{SENS} Mode

The three silicon prototypes presented in this chapter are developed with the aim of extend UB01 capabilities to cover some key aspects and important functionalities of gas sensing applications not addressed in the previous test-chip design. UB31, UB32 and UB33 are based on the same general oscillator readout principle and have been fabricated with the same standard Infineon 130 nm CMOS technology. In UB31 and UB32 different V2I biasing techniques are addressed, showing the differences between a grounded sensor or a double V2I configuration. Improved current mirrors design and multiplexing capabilities are also discussed. UB33 is the last test-chip developed in this project and adds a new readout mode in which is also possible to detect capacitive sensors with a similar approach used for the resistive readout.

4.1 UB31 and UB32

4.1.1 Sensor Biasing and Top-level Design

An important aspect to consider when designing resistance-based oscillator readouts is choosing the MOX sensor biasing strategy. It has been previously addressed that placing the sensor inside the oscillating circuit and thus having variable voltages on its terminals could decrease sensor performances, leading to worst gas sensitivity and worst linearity. For this reason the same biasing approach exploited in UB01 of having precise V2I buffers taking care of sensor biasing is

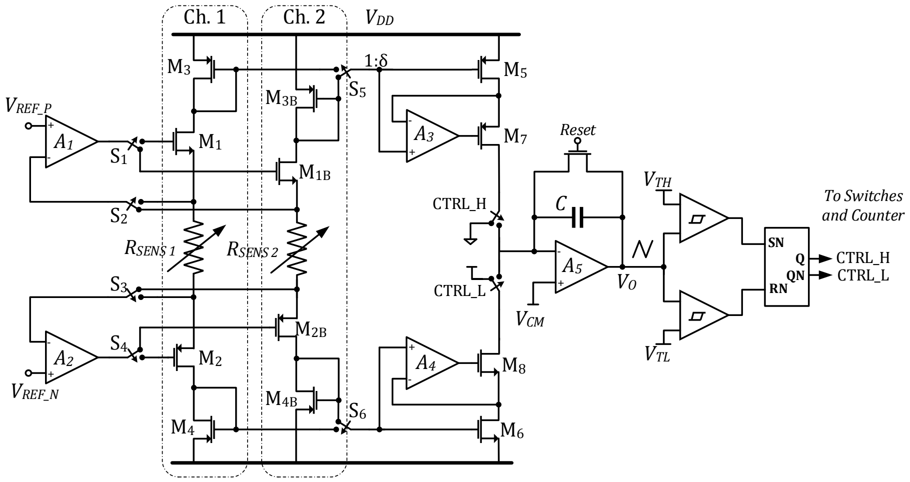

Figure 4.1: UB31 architecture: dual-channel, double V2I, R-to-T converter with digital output

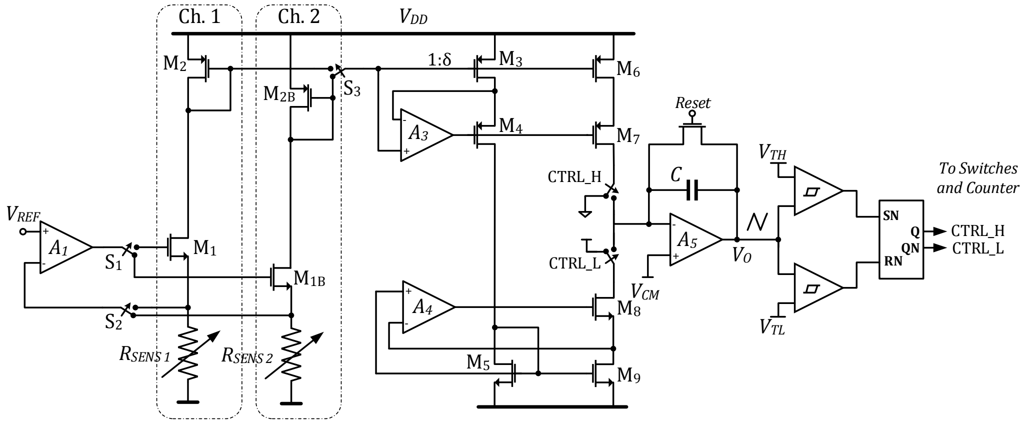

Figure 4.2: UB32 architecture: dual-channel, single V2I with grounded R_{SENS}, R-to-T converter with digital output

adopted for UB31-32. The V2I converter isolates the MOX form the oscillating part of the circuit maintaining a stable voltage biasing. It can be implemented using one Opamp in V2I configuration thus biasing only one terminal of the sensor (the second terminal could be grounded or connected to the power supply), or using two V2I Opamps, biasing both sensor terminals. Figure 4.1 and Figure 4.2 show UB31 and UB32 architectures respectively. UB31 exploits Opamps A_1 and A_2 to provide the double V2I sensor biasing, while UB32 uses only one Opamp (A_1 in Figure 4.2) and the second sensor terminal is connected to ground like the

UB01 architecture.

The double V2I strategy is the best to ensure optimal sensor performances since it isolates both MOX terminals from ground and supply noise. It requires two Opamps but it also requires one less current mirror branch. Transistors M_3, M_4 and M_5 in Figure 4.2 are needed to replicate the sensor current and perform the sign inversion, while in Figure 4.1 the current is taken from the negative sensor terminal through transistors M_2-M_4 and directly mirrored into M_6-M_8. One less mirror branch means less errors due to mirroring and less overall current consumption. Moreover the two-Opamp architecture further reduces impact of A_1 and A_2 offsets on the final measurement error, similarly to what explained for comparators offsets in section 2.2. Indeed V2I offset was a critical aspect of UB01 design because of the low V_{REF} value. In UB31 the basing voltage on the sensor is again only $V_{REF\_P} - V_{REF\_N} = 50\,\text{mV}$ to limit the sensor current to 500 µA, but matching between A_1 and A_2 limits voltage variations due to offsets (the same offset is applied at both R_{SENS} terminals) increasing robustness of the double V2I design.

In term of static power consumption the additional Opamp consumes only 5 µA of current. All V2I amplifiers in both UB31 and UB32 designs are based on the single-stage folded-cascoded topology described in subsection 3.1.1. However, to make the double V2I design possible, it is necessary to increase the power supply to 1.8 V to make room for the additional transistors; the two current conveyor M_1 and M_2 must be designed with very large W/L to keep their overdrive low and to avoid saturation of the outputs of amplifiers $A_{1\text{-}2}$ in high sensor current conditions. Moreover some MOX sensors do not have both their terminals accessible because one of the two needs to be grounded to the substrate to ensure proper functioning. In this case the single V2I biasing strategy remains the only possible solution.

Integrator and comparators of UB31 and UB32 are the same used in UB01 design, which are able of sustain a maximum oscillation frequency of $\approx 10\,\text{MHz}$. UB31 $R_{SENS}|_{min} = 100\,\Omega$, which is same value of the previous test-chip, while UB32 is optimized for slightly less conductive sensors and $R_{SENS}|_{min}$ is set at $10\,\text{k}\Omega$. The UB32 sensor current is consequently scaled by a two-decades factor by increasing V_{REF} to 500 mV and the mirroring ratio δ to 1:1, effectively changing the gain parameter α. This guarantees that both UB31 and UB32 have the same oscillation frequencies range of the previous design, a good trade-off between measurement time and power consumption. The additional sensor thermal noise due to the bigger R_{SENS} in UB32 is perfectly compensated by the increased voltage V_{REF} and the theoretical V2I SNR remains the same of UB01 and UB31 (Equation 2.11). Table 4.1 summarizes the main differences between the two test-chips.

Table 4.1: UB31 and UB32 top level design parameters

	UB31	UB32
Architecture	Double V2I	Single V2I
$R_{SENS}\|_{min}$	100 Ω	10 kΩ
$f_{OSC}\|_{max}$	10 MHz	10 MHz
V_{REF}	50 mV	500 mV
Mirroring ratio δ	1:10	1:1
Analog V_{DD}	1.8 V	1.5 V

4.1.2 Improved Current Mirrors

The current mirrors are implemented using the regulated cascode technique to further boost their output impedance and achieve better accuracy compared to the low voltage cascode mirrors of the previous design. The increased output impedance is obtained through the feedback loop provided by two high-gain Opamps (A_3 and A_4 in Figure 4.1 and Figure 4.2) which held the drains of mirror transistors at the same voltage of the references diodes. Again A_3 and A_4 are based on the single-stage folded cascode topology which ensure high DC gain (>90 dB) with minimal current consumption (5 µA) since they drive very high impedance nodes. The two Opamps differ from each other since A_3 is a p-input stage while A_4 is the complementary n-input to better fit the operating point constraints.

Figure 4.3 a simulation shows the relative error in the mirrored sensor current in worst-case PVT corners for the UB31 test-chip. The improved mirrors are able to process up to 5-decades of sensor resistance values without significant distortion and the actual lowest limit of mirrored sensor current is $\approx$ 500 pA. This means that R_{SENS} can be as big as 10 MΩ and successfully be converted if the measurement time is increased to 2.5 second. The extended time window is necessary to allow

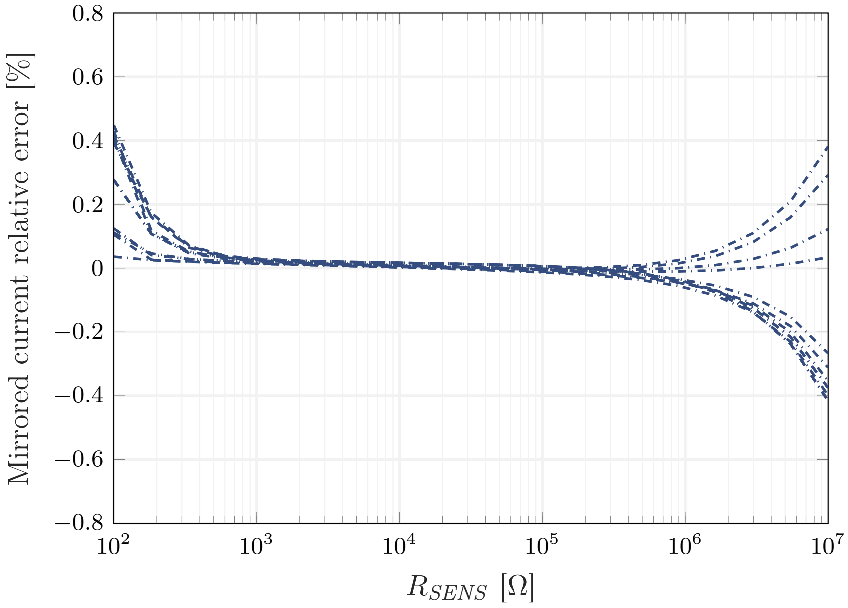

Figure 4.3: UB33 regulated cascoded mirrors relative error vs.R_{SENS} during PVT variations

the counters to reach the minimum count (256) needed to achieve the 8-bit digital precision. With the additional measurement time the ASIC can support then up to 148 dB of dynamic range. UB32 instead can cover only 138 dB ($\approx$ 4.5 decades of R_{SENS} with 8-bit precision) because of the errors introduced by the additional mirroring branch.

4.1.3 Multiplexing

A complete gas sensing system requires multiple MOX sensors to gather more information on the air composition and perform modern pattern recognition techniques. It is then important to ensure that the ASIC can be successfully connected to a matrix of different sensors through a multiplexed architecture. The introduction of a multiplexer can drastically affect the system resolution because of the unavoidable parasitic resistance of the switches necessary to select which sensor resistance to measure. This can be particularly evident when sensing very conductive MOX such as the target sensors of UB31 which can reaches resistance values as small as 100 Ω. In this scenario the voltage drop on the switches cannot be neglected if they are simply put in series with the sensor itself. Moreover using big switches to reduce the $r_{ds(on)}$ would solve the voltage drop problem

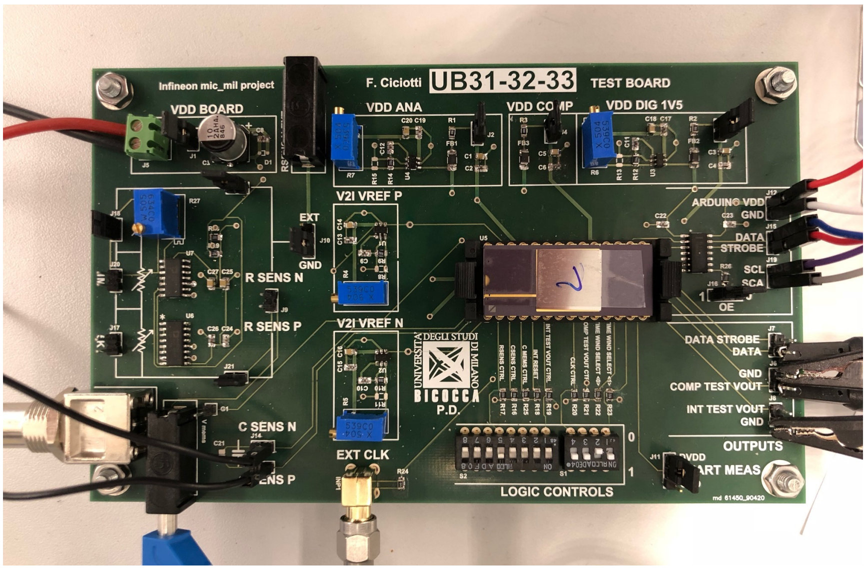

Figure 4.4: UB31, UB32 and UB33 test board

but the leakage current will then be comparable to the sensing current when the MOX resistance become very big. The adopted solution consists in placing the multiplexer switches outside of the current signal path, placing them in very high impedance nodes as shown in Figure 4.1 and Figure 4.1. Both UB31 and UB32 have two channels to test the multiplexed architecture. The V2I mirroring branch is replicated by transistors M_B and the two sensors $R_{SENS\ 1\text{-}2}$ are selected through switches $S_{1\text{-}6}$ in UB31 and $S_{1\text{-}3}$ in UB32.

The solution completely eliminates the switches parasitic problem and recovery time of current mirrors when disconnecting their gates when selecting different channels is negligible compared to the measurement time.

4.1.4 R_{SENS} Mode Characterization

UB31-32 are tested using the same methodology adopted to characterize UB01 described in section 3.2. Digitally programmable potentiometers are used to sweep the input sensor resistance for the whole DR and a photograph of the developed PCB test-board is shown in Figure 4.4.

Measurement results confirm the simulated performances, showing that the relative error in the sensor resistance estimation is between ±0.4 % for 5-decades of measured R_{SENS} for UB31 and about 4.5-decades for UB32 (Figure 4.5).

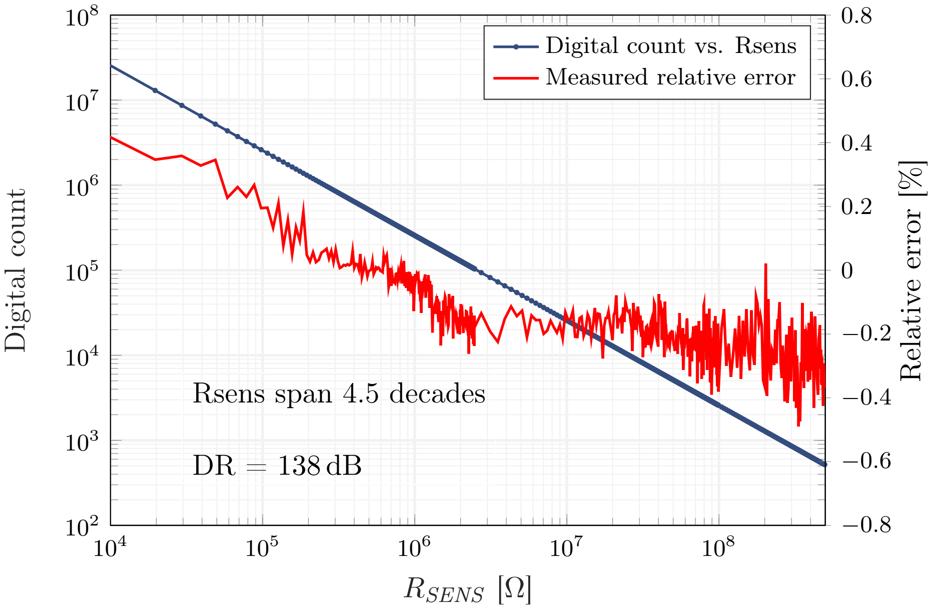

Figure 4.5: UB32 characterization: digital count value vs. R_{SENS} with measured relative error

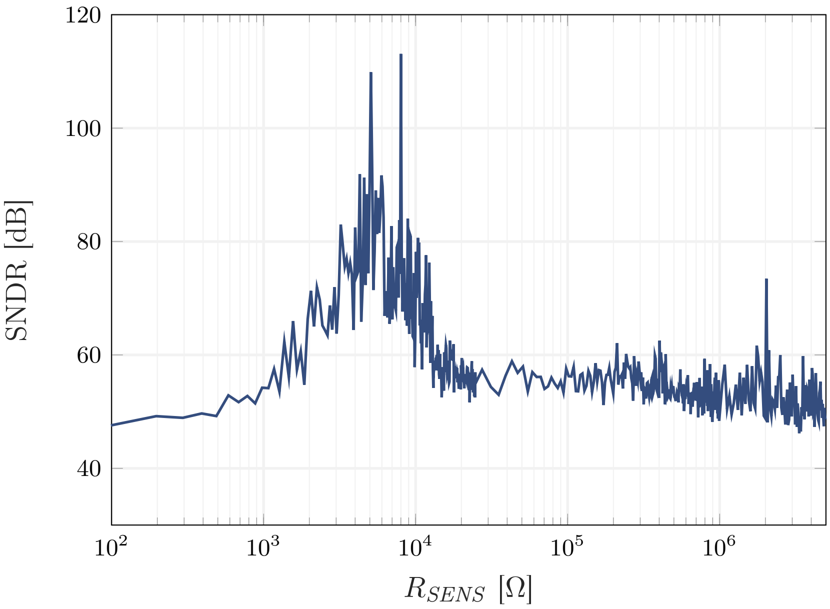

Figure 4.6: UB32 characterization: Signal to Noise and Distortion Ratio (SNDR) vs. R_{SENS}

4.2 UB33: C_{SENS} Mode

In chapter 1 the importance of improving gas sensing micro-systems including some sort of humidity sensor has been widely discussed. Typically, humidity sensor that satisfy the low-power, low-cost requirements and that can be integrated alongside MOX gas sensors are based on capacitive detection which is implemented through MicroElectroMechanical Systems (MEMS) sensors. Being able to use the same sensor interface used for MOX resistive readout to also detect MEMS capacitance would then avoid the development of a dedicated analog readout system avoiding to increase production costs and final device power consumption. UB33 introduces then a second operative mode that makes capacitive readouts possible.

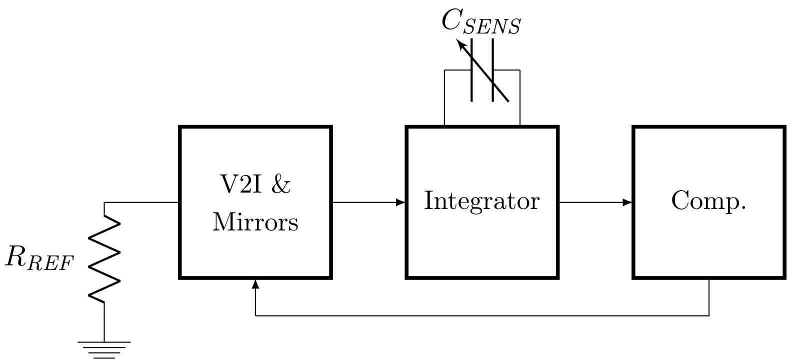

Figure 4.7: General oscillator architecture block diagram in C_{SENS} mode

Capacitance-to-Time

Equation 2.2 indicates that the oscillation period V_O of the adopted architectures actually depends on both resistance and capacitance value. In the resistance-to-time conversion principle, which up to this point was used to perform MOX resistive readout, the unknown parameter was R_{SENS}, and the capacitance value was fixed. Inverting the roles of resistance and capacitance allows then to use the same architecture (general block diagram in Figure 4.7) to measure an unknown capacitor and the oscillation period is then determined by the following equation.

$$T_{OSC} = \frac{2R_{REF} \cdot \Delta V}{\delta \cdot V_{REF}} \cdot C_{SENS} = \alpha \cdot C_{SENS} \tag{4.1}$$

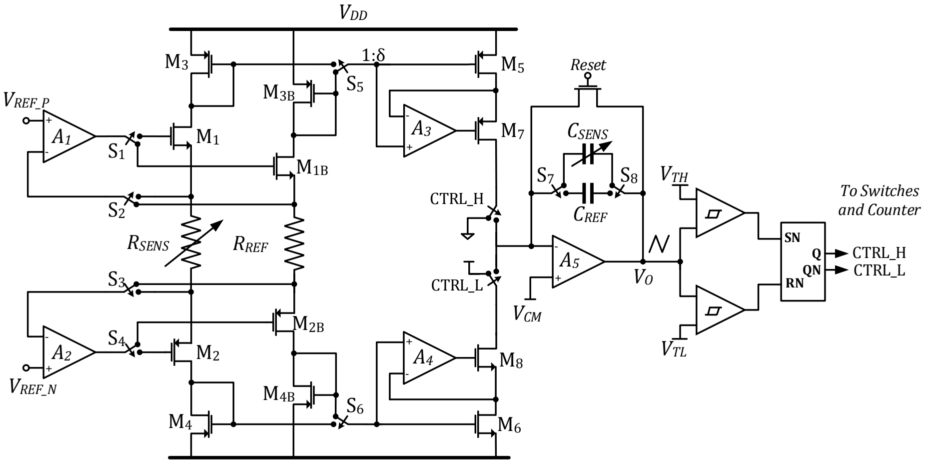

Figure 4.8: UB33 architecture: dual-mode R-to-T and C-to-T converter with digital output

UB33 (architecture shown in Figure 4.8) allows to disconnect the readout interface from the resistive sensor and to connect it to a reference resistor R_{REF}. This generates a constant current I_{SENS} which is then integrated in the sensor capacitance C_{SENS} leading to an oscillation frequency proportional to C_{SENS} itself. The switches to choose between R_{SENS} and R_{REF} are implemented with the same multiplexing strategy previously described to avoid parasitic effects while switches $S_{7\text{-}8}$ are used to connect the reference capacitance or the sensor capacitance to the integrator. Careful $S_{7\text{-}8}$ design is mandatory since big $r_{ds(on)}$ in series with the capacitance can cause a non-linear output voltage behavior. Also $S_{7\text{-}8}$ switches can't be designed too big (to reduce $r_{ds(on)}$) because of their parasitic capacitance that could become comparable with the integrator capacitance value.

Target sensors have typically nominal capacitance in the few pF range and usually require detection in the fF or sub-fF range, a much higher resolution compared to the minimum 8-bits used in the R_{SENS} measurements. The time domain approach, which was the best solution to cover the very wide DR of MOX sensors, can also be effective in the measurement of a capacitance. Indeed, sufficiently long measurement times allows to increase the number of counted oscillation reducing quantization error and also reducing impact of withe noise.

The parameter α in Equation 4.1 is set at $320\,\mathrm{ns\,pF^{-1}}$ by choosing $R_{REF}{=}1\,\mathrm{k\Omega}$ and obtaining a constant current of $5\,\mu\mathrm{A}$. This leads to oscillations in the MHz range, a good trade-off between speed and power consumption. A relatively small R_{REF} value allows also to boost V2I SNR. Moreover the regulated cascode current mirrors have optimal performances close to that resistance value, avoiding to add additional error and distortion in the capacitance measurement.

Digital programmability in the control logic allows re-configuring counters for the C_{SENS} mode measurements and the time window is set to 100 ms, guaranteeing a digital output data rate of 10 Hz, fast enough for this application, and sufficiently high SNR. The minimum number of bits allocated for the digital output resolution is increased from 8 to 13.

4.3 C_{SENS} Mode Characterization

4.3.1 MEMS

Similarly to MOX sensors, MEMS development started more than sixty years ago and evolved from very early visions and bulky prototypes to complex miniaturized devices which take advantages of the new nanoscale technologies. Nowadays they are used in many applications and can be found in systems ranging from automotive, medical, chemical, industrial and consumer applications [34], [35].

Capacitive sensing is one of the most important and widely used sensing mechanisms and mostly relies on structures resembling a parallel-plate capacitor. Usually MEMS are composed by one fixed conductive plate on one side and a moving conductive plate on the other side, leading to a capacitance equal to:

$$C = \frac{\varepsilon_0 \varepsilon_r A}{d} \tag{4.2}$$

where ε_0 and ε_r are permittivity of free space and relative permittivity of material between the plates respectively. A is the area of the overlapping plates and d their distance. The capacitive variation can then be caused by the displacement of the moving suspended microscopic plate in the presence of an external applied force (e.g. pressure, voltage) or by the chance of permittivity (e.g humidity in the air).

The characterization of UB33 has been performed using real capacitive MEMS sensors provided by Infineon [36]. These sensors are typically used as microphones to detect atmospheric pressure variations due to the sound waves presence. They are divided in two categories: single back plate or dual back plate (Figure 4.9). In both structures the back-plates are fixed and the membrane moves; the advantage

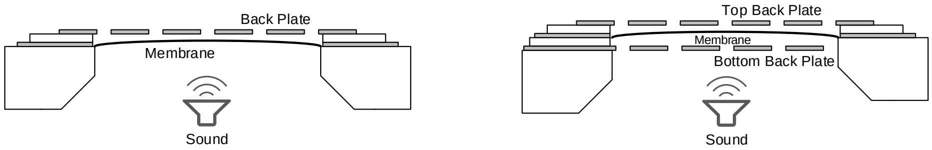

(a) Single back plate **(b)** Dual back plate

Figure 4.9: MEMS cross-section

of Infineon dual back plate MEMS technology is that it allows a differential capacitve readout, higher biasing voltages and it increases THD.

4.3.2 Experimental Setup and Pull-in Voltage

Testing UB33 in C_{SENS} mode using actual sound waves or pressure as input signals requires a complex setup consisting in a vacuum cup that creates the isolated chamber for pressure testing. Since the purpose of this characterization is only to demonstrate the proper ASIC functioning and its ability to sense MEMS capacitance variation, the input signal nature is not very important. It is only necessary to generate a controlled capacitance variation and confront it with the readout value obtained by the ASIC.

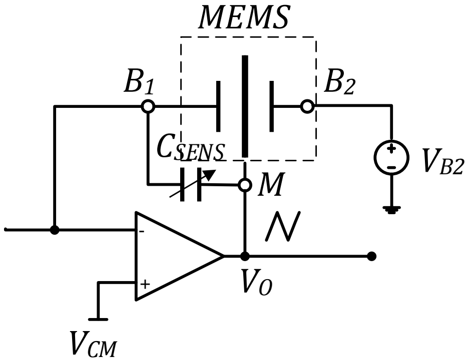

Figure 4.10: Schematic of UB33 integrator bonded to a dual back-plate MEMS

To generate the capacitance variation, a dual back-plate MEMS is placed in the same package of the ASIC and bonded to it as shown in Figure 4.10. The bottom back-plate terminal B_1 is connected to the virtual ground of the integrator,

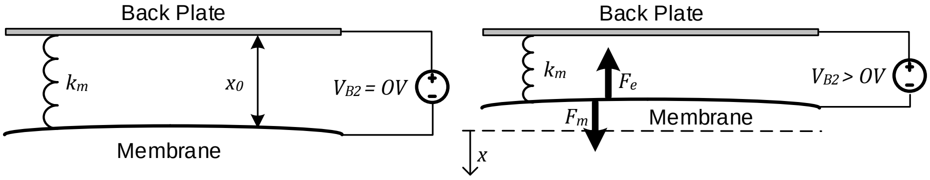

Figure 4.11: Equilibrium position of MEMS without or with electrical bias

while the flexible membrane terminal M is connected to the output node V_O of the integrator. The top back-plate terminal B_2 is left accessible form the outside and then connected to an external precise voltage generator V_{B2}. By increasing V_{B2} the membrane is pulled toward the top back-plate, effectively reducing the value of the capacitance C_{SENS} between the bottom back-plate and the membrane itself.

The position of the MEMS membrane is determined by the equilibrium between the electrostatic attractive force F_e caused by the driving voltage V_{B2} and the elastic restoring force of the membrane itself, namely the mechanical spring force F_m. Referring to the diagram in Figure 4.11, which shows the membrane position in a single back-plate MEMS (for simplicity) with or without biasing, the electrostatic force is then:

$$F_e = \frac{1}{2}\frac{C(x)V_B^2}{x_0 + x} \tag{4.3}$$

where $x_0 + x$ is the distance d between the plates and C the capacitance which is also a function of x (Equation 4.2). The mechanical spring force is:

$$F_m = -k_m x \tag{4.4}$$

and the membrane equilibrium position is obtained imposing F_e=F_m.

$$-k_m x = \frac{1}{2}\frac{C(x)V_B^2}{x_0 + x} \tag{4.5}$$

The previous equation can be expanded, yielding to a quadratic equation for x:

$$x^2 + x_0 x + \frac{C(x)V_B^2}{2k_m} = 0 \tag{4.6}$$

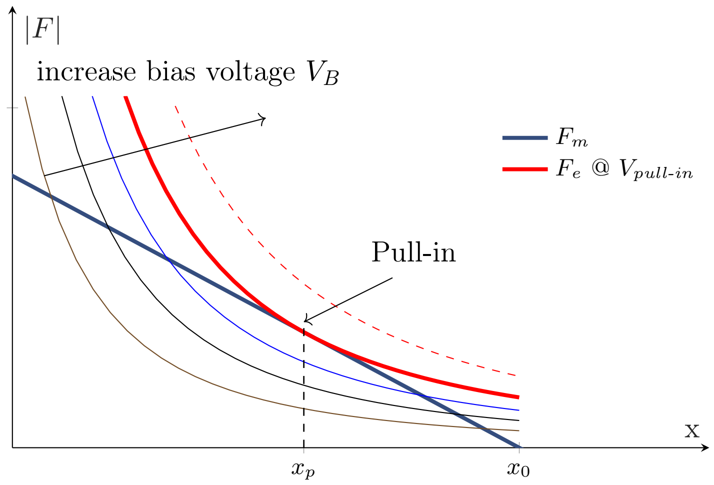

Figure 4.12: Graphic representation of equilibrium position in MEMS

The solutions of Equation 4.6 are graphically shown in Figure 4.12. The blue straight line represent the mechanical spring force, while the other curves the electrostatic force at different driving voltage values. For low driving voltage values there are two possible solutions and only one represent the stable equilibrium point (on the right). As V_B increases, F_e increases, and the membrane moves further away from x_0 until eventually a 'critical point' x_p where there is only one solution is reached. This condition is called *pull-in* and after this point the spring force can no longer contend with the electrostatic fore and the membrane is thrown off balance.

The pull-in voltage $V_{pull\text{-}in}$ is a critical parameter in MEMS characterization and the determination of its value is one of the parameters used for UB33 characterization. ASIC biasing and data acquisition are performed with the same board and methodology described above for the R_{SENS} mode and the acquired results are confronted with Infineon data-sheets and simulation models (mainly nominal capacitance value, ΔC and $V_{pull\text{-}in}$). Three different MEMS (models E2223, E2224 and E2290) with different sizes and capacitance values are bonded to different samples of UB33 to increase statistics. In Figure 4.13 a picture shows one of the samples bonded to the MEMS E2223.

4.3.3 Measurement Results

Measurements results of different samples of UB33 bonded to different MEMS are reported in the next plots. Figure 4.14, Figure 4.15 and Figure 4.16 show

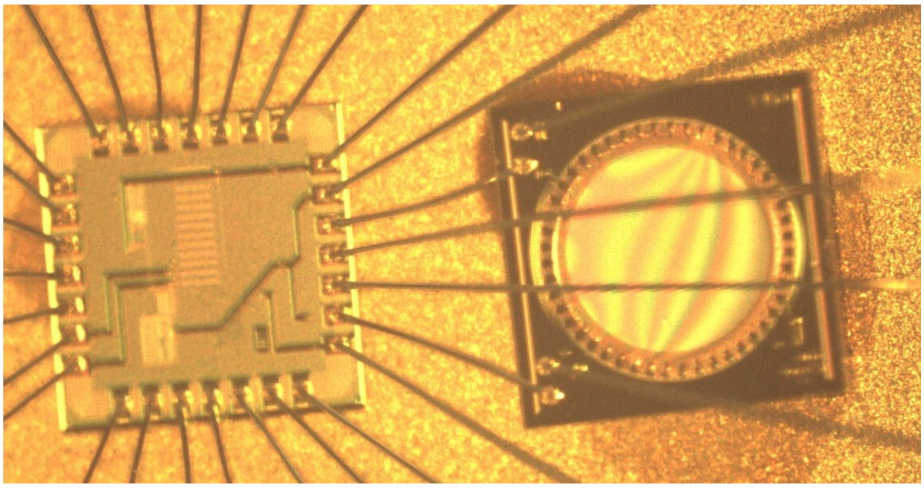

Figure 4.13: UB33 bonded to a dual back-plate MEMS sensor (model E2223)

measured C_{SENS} values when linearly sweeping the top back-plate voltage every 100 ms.

All three plots display the expected behavior and the measured capacitance decreases (recalling that the actual measured C_{SENS} is the capacitance between the membrane and the bottom back-plate and not between membrane and top back-plate) as the driving voltage V_{B2} is increased. Actually a minor C_{SENS} increase can be observed for V_{B2} between 0 V and 0.8 V and the maximum measured capacitance value is right around V_{B2}=800 mV. This behavior can be explained recalling that the bottom back-plate and the membrane are actually biased at the same common-mode voltage of the integrator Opamp virtual ground (V_{B1}=V_M=V_{CM}=0.8 V) and this creates a reverse-bias that pushes the membrane closer to the bottom back-plate until the positive biasing condition is reached (V_{B2}>800 mV). Actually the membrane biasing voltage is not statically fixed at the same value of integrator common-mode voltage, but it moves in the 0.4 V to 1.2 V range, being connected to the triangular output voltage V_O of the integrator. V_O oscillation, however, is at very high frequencies compared to the time necessary to actually move the MEMS membrane, and its effect on the MEMS behavior can effectively be neglected. Nominal capacitance values detected are ≈ 3.43 pF, ≈ 2.15 pF and ≈ 5.05 pF for MEMS E2223, E2224 and E2290 respectively, values that are in line with expected results considering typical technological spread of MEMS fabrication process (at least three sample for each MEMS model have been tested).

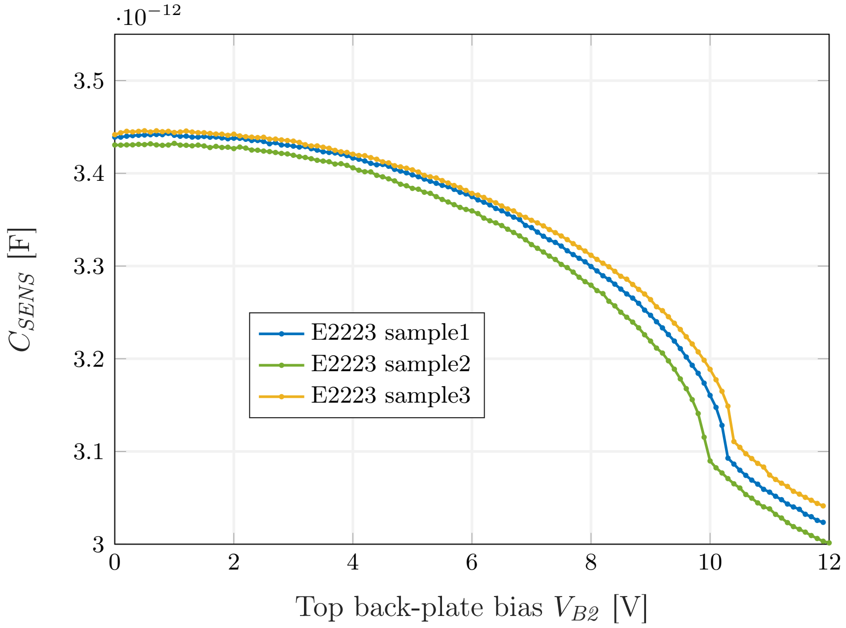

Figure 4.14: UB33 characterization with MEMS E2223: measured capacitance vs. top back-plate voltage

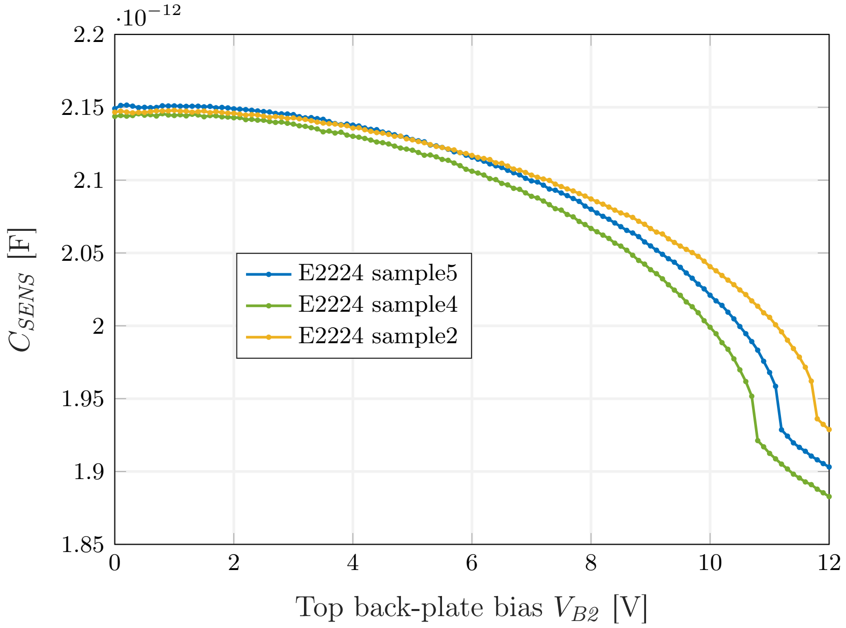

Figure 4.15: UB33 characterization with MEMS E2224: measured capacitance vs. top back-plate voltage

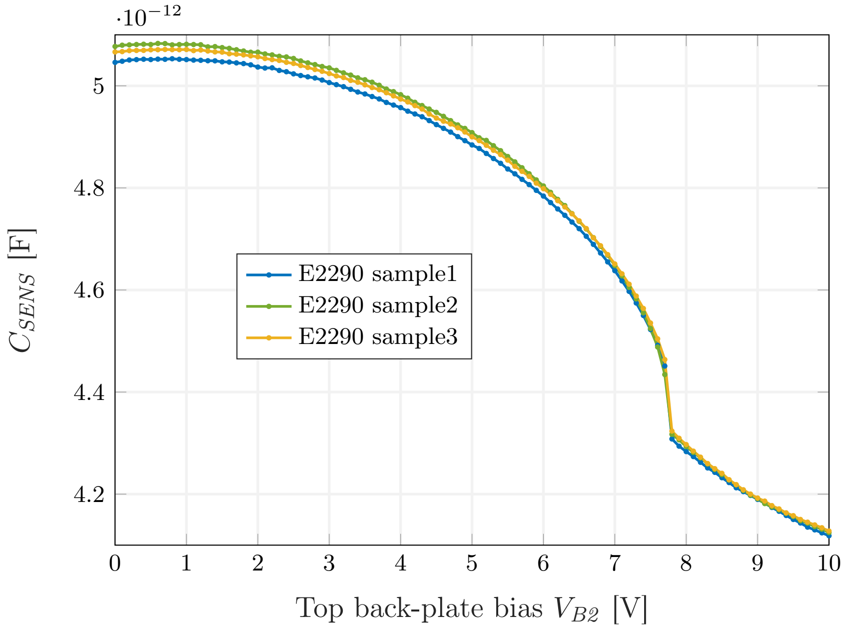

Figure 4.16: UB33 characterization with MEMS E2290: measured capacitance vs. top back-plate voltage

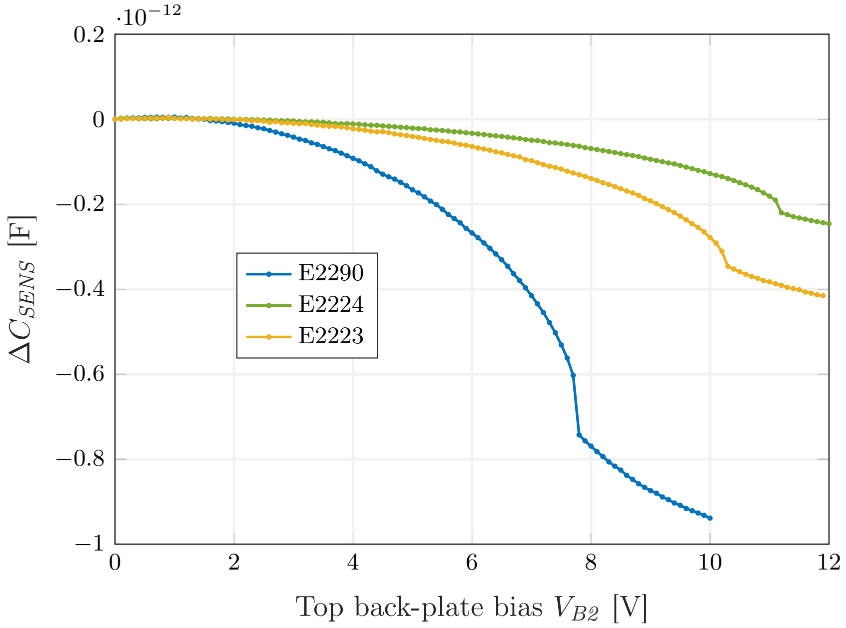

Figure 4.17: UB33 characterization: average ΔC_{SENS} measured vs. top back-plate voltage for E2223, E2224 and E2290

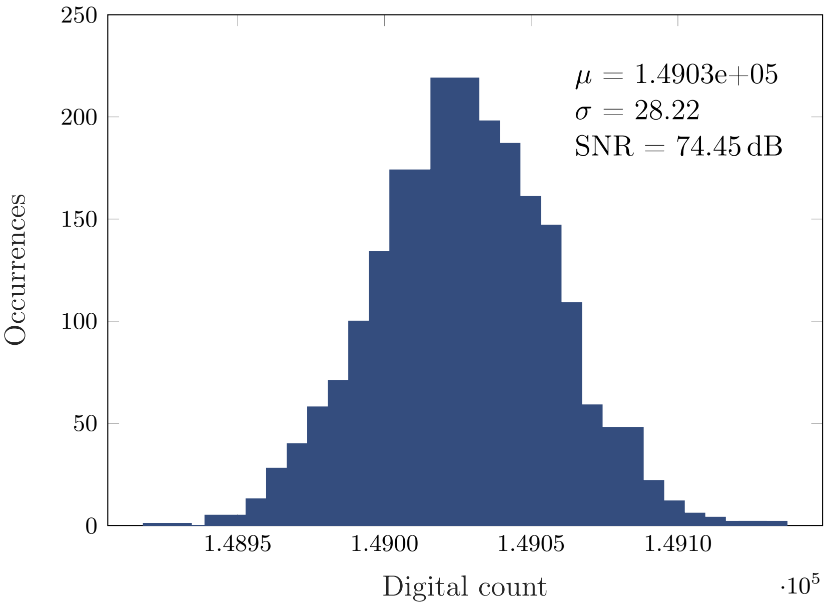

Figure 4.18: Noise persistence histogram plot in C_{SENS} mode. 2000 acquisitions

Pull-in voltages can be easily determined because of the abrupt capacitance variation when the condition is reached (well visible in Figure 4.14, Figure 4.15 and Figure 4.16) and the three $V_{pull\text{-}in}$ values are $\approx 10\,\mathrm{V}$, $\approx 11\,\mathrm{V}$ and $\approx 7.5\,\mathrm{V}$ where the 800 mV offset has also been taken in consideration. MEMS 2290, which is the biggest one, exhibits the highest capacitance variation from the nominal condition and the measured ΔC_{SENS} at $V_{pull\text{-}in}$ is about 0.7 pF. The other two have much smaller dimension and ΔC_{SENS} are 350 fF and 200 fF respectively for E2223 and E2224 (Figure 4.17).

The histogram plot in Figure 4.18 is obtained acquiring 2000 samples of the digital output code when sensing E2224 with 800 mV of driving voltage (nominal condition) to underline random noise in the ASIC. The obtained SNR is $\approx 74\,\mathrm{dB}$ meaning that the minimum detectable capacitance variation is about 400 aF which guarantees enough accuracy for the target applications.

UB33 has been tested with MEMS capacitance values in the pF range but it can successfully readout capacitance from 300 fF to $\approx 38\,\mathrm{pF}$. The minimum capacitance value is again limited by the maximum recommended oscillation frequency supported by the ASIC (10 MHz) which is the same maximum frequency supported in R_{SENS} mode. The maximum capacitance value depends on output data rate and resolution requirements of the digital logic (Equation 2.4), since the principle behind the time-to-digital conversion is always the same as in the resistive mode. Recalling that the measurement time is 100 ms and that the minimum number of bits allocated for the digital resolution is 13 (quantization noise should not dominate total SNR performances), the maximum oscillation period is:

$$T_{OSC}|_{max} = \frac{100\,\mathrm{ms}}{2^{13}} = 12.2\,\mathrm{\mu s} \tag{4.7}$$

and

$$C_{SENS}|_{max} = \frac{T_{OSC}|_{max}}{\alpha} = 38.12\,\mathrm{pF} \tag{4.8}$$

UB33 Dynamic range in C_{SENS} mode is then about 116 dB.

UB33 is also tested in R_{SENS} mode and performs identically to UB31 since both test-chips shares the identical resistive readout architecture.

4.4 Conclusions

In this chapter three additional silicon prototypes have been presented and discussed. The core of UB31, UB32 and UB33 is the same oscillator-based readout interface with digital output developed in the first prototype (UB01) which guarantees simple and cheap industrial implementation. UB01 already was able to satisfy most of the requirements dictated by modern gas sensing standards, being able to provide 128 dB of dynamic range with a maximum measured relative error of ±0.4 % at 4 Hz digital output data rate. In the new prototypes the dynamic range can be extended up to 138 dB (UB32) or 148 dB (UB31-33) at the cost of a lower output data rate (0.4 Hz) but most importantly the possibility to select different MOX sensor through a multiplexed architecture has been introduced. The multiplexed architecture has been implemented inserting all switches at high impedance nodes thus avoiding performances degradation. It works for both grounded (UB32) and double V2I (UB31-33) MOX sensor biasing strategies.

Moreover UB33 is fully compatible with capacitive sensors. Indeed the ASIC can be reprogrammed to perform capacitive readout exploiting the same oscillator-based approach used for MOX resistive readout. UB33 can manage 116 dB of dynamic range in C_{SENS} mode, being able to convert capacitance in the 0.3 pF to 38 pF range with an SNR of 74 dB and a digital output data rate of 10 Hz. Common specifications for MEMS capacitive sensors. The final performances of UB31, UB32 and UB33 are summarized in Table 4.2.

Table 4.2: UB31 UB32 and UB33 performances resume

	UB31	UB32	UB33
R_{SENS} range	100 Ω - 10 MΩ	10 kΩ - 500 MΩ	100 Ω - 10 MΩ
Max relative error	±0.4 %	±0.4 %	±0.4 %
DR @ 4 Hz	128 dB	128 dB	128 dB
DR @ 0.4 Hz	148 dB	138 dB	148 dB
Support multiplexing	yes	yes	yes
C_{SENS} range	-	-	300 fF - 38 pF
C_{SENS} mode SNR	-	-	74 dB
C_{SENS} mode DR	-	-	116 dB @ 10 Hz
Power consumption	840 µW@1.8 V	690 µW@1.5 V	840 µW@1.8 V

UB33 has been tested in C_{SENS} mode using real MEMS provided by Infineon. The experimental characterization confirms simulated ASIC performances and proves feasibility of the design in real applications

Chapter 5

Conclusions

In this work several oscillator-based, resistance-to-digital interfaces for MOX sensors have been presented and discussed. All developed prototypes have been carefully tested and evaluated and measurement results confirm that the developed ASICs are able to satisfy modern requirements in the gas sensing industry for mobile applications. Indeed, large dynamic range, large accuracy, low power consumption and fast measurement requirements have been met, solving the typical measurement time slowness of oscillator-based readout approaches with aggressive design strategies and system-level optimization. The oscillation frequencies have been boosted to achieve fast output data rates, maintaining minimal power consumption. Low-cost is guaranteed by the simplicity of the architecture, which uses only a single measurement scale, and by the simplicity of the integrated digital logic.

This work has also addressed the multiplexing problem, showing how it is possible to implement it without performances degradation, allowing readouts from multiple MOX sensors. This, and the addition of capacitive sensor support, makes the last developed ASIC (UB33) fully compatible with a complete gas sensing micro-system. UB33 allows to retrieve information from multiple different sensors, both resistive and capacitive, to improve pattern recognition algorithms and gas discrimination.

Table 5.1: State-of-the-art performances comparison

	[29]	[30]	[31]	[32]	UB33
R_{SENS} range	1 kΩ - 100 MΩ	100 kΩ - 10 GΩ	10 kΩ - 100 GΩ	1 kΩ - 10 GΩ	100 Ω - 1 MΩ
Max relative error	0.8 %	$\approx$ 0.9 %	$\approx$ 1 %	$\approx$ 5 %	0.4 %
Data Rate	0.1 Hz	$\approx$ 0.01 Hz	$<$ 0.01 Hz	33 Hz	4 Hz
Capacitive sensors support	no	no	yes*	no	yes
C_{SENS} range	-	-	few pF	-	300 fF - 38 pF
C_{SENS} mode SNR	-	-	-	-	74 dB
Power consumption	15 mW@3.3 V	$\gg$ 1 mW@3.3 V	-	25 mW@3.3 V	840 µW@1.8 V

* Only parasitic capacitance of MOX sensor

The state-of-the-art review has shown that none of the solutions proposed in literature is able to fully satisfy all target requirements yet, mostly because many of them are too complex and power hungry for portable devices or are not able to provide the necessary data rate. In Table 5.1 on page 64, several other oscillator-based architectures are compared, highlighting the competitiveness of the solutions developed in this thesis.

The architectures presented in this work have been developed targeting gas sensing application. However, the proposed approaches exhibit great versatility and can be easily adapted and used in other scenarios. Indeed, the trend in modern consumer electronic is to integrate lots of different sensors (pressure, temperature, gas, humidity, microphones,...) in a single device. Each sensor is based on different physical principles which translate in different electrical quantities to be detected (mainly resistance and capacitance). A flexible and cheap readout architecture (UB33), compatible with a wide range of resistive and capacitive sensors, could avoid the design of different readout analog systems that need to be adapted to different sensors, decreasing production costs and final devices power consumption.

Appendix A

Digital Logic & VHDL Code

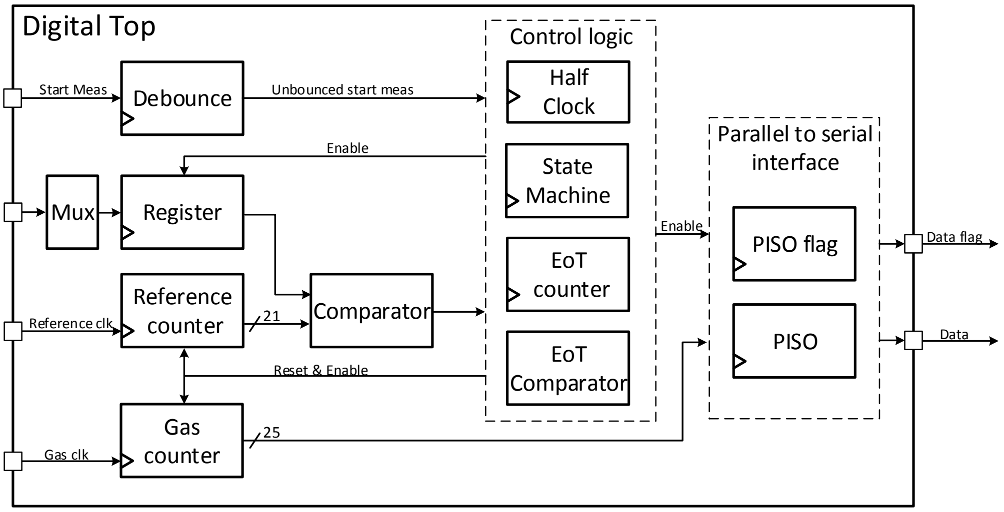

Figure A.1: Simplified functional block diagram of Digital Top

ASIC digital logic is implemented with synthesis of VHDL code. A simplified functional block diagram of the top level architecture *Digital Top* is represented in Figure A.1. The start measurement signal is debounced (to ensure that a stable state is reached) before feeding it to the control logic. The two counters are driven by a reference clock running at 500 kHz and by the gas signal coming from the oscillator. A multiplexer and a register are used to select different time-windows which are then compared to the reference counter to determine the measurement duration. The content of the gas counter is serially transmitted to the output by a means of a parallel-to-serial- interface implemented with two shift register.

The Parallel-In Serial-Out (PISO) register transmits R_{SENS} information, while PISO flag is used as a strobe signal for easier data acquisition. The control logic is implemented with a state machine block and a clock divider is also used for signals synchronization. Two additional block, End od Transmission (EoT) counter and comparator are used for timing the parallel-to-serial interface.

The VHDL source codes of each block are listed below.

Listing A.1: Digital Top

```
library ieee;
use ieee.std_logic_1164.all;
use ieee.numeric_std.all;

entity digital_top is
    port(
        system_clk              :in std_ulogic;
        gas_clk                 :in std_ulogic;
        start_meas              :in std_ulogic;
        time_wind_select        :in std_ulogic_vector (1 downto 0);
        data_flag               :out std_ulogic;
        serial_data_out         :out std_ulogic
        );
end digital_top;

architecture rtl of digital_top is
    component half_clk is
        port(
            system_clk              :in std_ulogic;
            half_clk                :out std_ulogic
            );
    end component ;

    component control_logic is
        port(
            start_meas          :in std_ulogic;
            clk                 :in std_ulogic;
            comp_in             :in std_ulogic;
            end_of_trasm        :in std_ulogic;
            eot_count_enable    :out std_ulogic;
            count_enab          :out std_ulogic;
            count_reset         :out std_ulogic;
            load_register       :out std_ulogic;
            register_enable     :out std_ulogic
            );
    end component;

    component counter is
        generic(
                Nbits           :positive;
                MaxCount        :positive);
        port(
            reset               :in std_ulogic;
            clk                 :in std_ulogic;
            enable              :in std_ulogic;
            out_count           :out std_ulogic_vector(Nbits-1 downto 0)
            );
    end component;

    component reg is
        port(
            input           :in std_ulogic_vector(20 downto 0);
            enable          :in std_ulogic;
            clk             :in std_ulogic;
            output          :out std_ulogic_vector(20 downto 0)
```

```
          );
  end component;

  component mux is
      port(
          a         :in std_ulogic_vector(20 downto 0);
          b         :in std_ulogic_vector(20 downto 0);
          c         :in std_ulogic_vector(20 downto 0);
          d         :in std_ulogic_vector(20 downto 0);
          sel       :in std_ulogic_vector(1 downto 0);
          output    :out std_ulogic_vector(20 downto 0)
          );
  end component;

  component debounce is
      generic(
              counter_size  :  integer := 13);
      port(
          clk     : in  std_ulogic;
          button  : in  std_ulogic;
          result  : out std_ulogic
          );
  end component;

  component PISO is
      port(
          system_clk          :in std_ulogic;
          enable              :in std_ulogic;
          data_in             :in std_ulogic_vector(24 downto 0);
          serial_data_out     :out std_ulogic
          );
  end component ;

  component PISO_flag is
      port(
          system_clk          :in std_ulogic;
          enable              :in std_ulogic;
          serial_data_out     :out std_ulogic
          );
  end component ;

  component comparator is
      port(
          a           :in std_ulogic_vector(20 downto 0);
          b           :in std_ulogic_vector(20 downto 0);
          out1        :out std_ulogic
          );
  end component;

signal unbounced_start_meas_sig : std_ulogic;
signal comparator_sig : std_ulogic;
signal count_enable_sig : std_ulogic ;
signal eot_count_enable_sig : std_ulogic ;
signal count_reset_sig : std_ulogic ;
signal load_register_sig : std_ulogic;
signal register_enable_sig : std_ulogic;
signal out_count_gas_sig : std_ulogic_vector (24 downto 0);
signal out_count_system_sig : std_ulogic_vector (20 downto 0);
signal data_flag_sig : std_ulogic;
signal out_count_eot_sig : std_ulogic_vector (20 downto 0);
signal eot_flag_sig : std_ulogic;
signal time_window : std_ulogic_vector (20 downto 0);
signal half_clk_sig : std_ulogic;
signal time_window_final : std_ulogic_vector (20 downto 0);

constant time_window1 :std_ulogic_vector (20 downto 0):="001111010000100100000";
constant time_window2 :std_ulogic_vector (20 downto 0):="100110001001011010000";
constant time_window3 :std_ulogic_vector (20 downto 0):="000001100001101010000";
constant time_window4 :std_ulogic_vector (20 downto 0):="000011110100001001000";
constant eot :std_ulogic_vector (20 downto 0):="000000000000000011001";

  begin
```

```
data_flag<=data_flag_sig;

half_clk1:half_clk
port map (system_clk => system_clk,
           half_clk => half_clk_sig);

debounce1:debounce
port map( clk => half_clk_sig,
          button => start_meas,
          result => unbounced_start_meas_sig);

control_logic1:control_logic
port map( start_meas           => unbounced_start_meas_sig,
          clk                  => half_clk_sig,
          omp_in               => comparator_sig,
          end_of_trasm         => eot_flag_sig,
          eot_count_enable     => eot_count_enable_sig,
          count_enable         => count_enable_sig,
          count_reset          => count_reset_sig,
          load_register        => load_register_sig,
          register_enable      => register_enable_sig);

mux1:mux
port map( a               => time_window1,
          b               => time_window2,
          c               => time_window3,
          d               => time_window4,
          sel             => time_wind_select,
          output          => time_window);

reg1:reg
port map( input            => time_window,
          enable           => register_enable_sig,
          clk              => system_clk,
          output           => time_window_final);

gas_counter:counter
generic map (25, 33554431)
port map( reset             => count_reset_sig,
          clk               => gas_clk,
          enable            => count_enable_sig,
          out_count         => out_count_gas_sig);

system_counter:counter
generic map (21, 2097151)
port map( reset             => count_reset_sig,
          clk               => system_clk,
          enable            => count_enable_sig,
          out_count         => out_count_system_sig);

end_of_trasmission_counter:counter
generic map (21, 11001)
port map( reset             => count_reset_sig,
          clk               => data_flag_sig,
          enable            => eot_count_enable_sig,
          out_count         => out_count_eot_sig);

PISO1:PISO
port map( system_clk        => half_clk_sig,
          enable            => load_register_sig,
          data_in           => out_count_gas_sig,
          serial_data_out   => serial_data_out);

PISO_flag1:PISO_flag
port map( system_clk        => system_clk,
          enable            => load_register_sig,
          serial_data_out   => data_flag_sig);

comparator1:comparator
port map( a       => out_count_system_sig,
          b       => time_window_final,
          out1    => comparator_sig);
```

```
    comparator_eot:comparator
    port map( a       => out_count_eot_sig,
              b       => eot,
              out1    => eot_flag_sig);

  end rtl;
```

Listing A.2: Control logic state machine

```
entity control_logic is
    port(
        start_meas          :in std_ulogic;
        clk                 :in std_ulogic;
        comp_in             :in std_ulogic;
        end_of_trasm        :in std_ulogic;
        eot_count_enable    :out std_ulogic;
        count_enable        :out std_ulogic;
        count_reset         :out std_ulogic;
        load_register       :out std_ulogic;
        register_enable     :out std_ulogic
        );
end control_logic;

architecture rtl of control_logic is
    type State_type is (idle, gas_count, data_out);
    signal State : State_Type;
begin
    process (clk, start_meas)
        begin
            If (start_meas = '0') then
            State <= idle;
            elsif rising_edge(clk) then
                case State is
                    when idle =>
                        if start_meas='1' then
                        State <= gas_count;
                        end if;
                    when gas_count =>
                        if comp_in='1' then
                        State <= data_out;
                        end if;
                    when data_out =>
                        if end_of_trasm='1' then
                        State <= idle;
                        end if;
                    when others =>
                        State <= idle;
                end case;
            end if;
    end process;

    count_enable <= '1' when State=gas_count else '0';
    eot_count_enable <= '1' when State=data_out else '0';
    count_reset <= '1' when State=idle else '0';
    load_register <= '0' when State=data_out else '1';
    register_enable <= '1' when State=idle else '0';

end rtl;
```

Listing A.3: Counter

```
entity counter is
    generic (
            Nbits                 :positive;
            MaxCount              :positive);
    port(
        reset               :in std_ulogic;
        clk                 :in std_ulogic;
        enable              :in std_ulogic;
        out_count           :out std_ulogic_vector(Nbits-1 downto 0)
```

```
        );
end counter;

architecture rtl of counter is
    signal count: unsigned(Nbits-1 downto 0);
begin
    process(reset,clk)
        begin
            if reset ='1' then
            count<=(others=>'0');
            elsif rising_edge(clk) and enable='1' then
                if count = MaxCount then
                count <= (others => '1');
                else
                count <= count + 1;
                end if;
            end if;
    end process;

  out_count<=std_ulogic_vector(count);
end rtl;
```

Listing A.4: Comparator

```
entity comparator is
    port(
        a       :in std_ulogic_vector(20 downto 0);
        b       :in std_ulogic_vector(20 downto 0);
        out1    :out std_ulogic
    );
end comparator;

architecture rtl of comparator is
    begin
        process (a,b)
            begin
                if a >= b then
                out1 <= '1';
                else
                out1 <= '0';
                end if;
        end process;
end rtl;
```

Listing A.5: Debounce

```
entity debounce is
    generic(
            counter_size  :  integer := 13);
    port(
        clk     : in  std_ulogic;
        button  : in  std_ulogic;
        result  : out std_ulogic
        );
end debounce;

architecture rtl of debounce is
    signal flipflops   : std_ulogic_vector(1 downto 0);
    signal counter_set : std_ulogic;
    signal counter_out : unsigned(counter_size-1 downto 0) := (others => '0');
begin
counter_set <= flipflops(0) xor flipflops(1);
    process(clk)
        begin
            if rising_edge (clk) then
            flipflops(0) <= button;
            flipflops(1) <= flipflops(0);
                if(counter_set = '1') then
                counter_out <= (others => '0');
                elsif(counter_out(counter_size-1) = '0') then
```

```
                counter_out <= counter_out + 1;
                else
                result <= flipflops(1);
                end if;
            end if;
    end process;
end rtl;
```

Listing A.6: Half clock

```
entity half_clk is
    port(
        system_clk            :in std_ulogic;
        half_clk              :out std_ulogic );
end half_clk ;

architecture rtl of half_clk is
signal clk_temp : std_ulogic := ’0’;
begin
    process(system_clk)
        begin
            if rising_edge(system_clk) then
            clk_temp <= not clk_temp;
            end if;
    end process;
    half_clk<=clk_temp;
end rtl;
```

Listing A.7: Mux

```
entity mux is
    port(
        a       :in std_ulogic_vector(20 downto 0);
        b       :in std_ulogic_vector(20 downto 0);
        c       :in std_ulogic_vector(20 downto 0);
        d       :in std_ulogic_vector(20 downto 0);
        sel     :in std_ulogic_vector(1 downto 0);
        output  :out std_ulogic_vector(20 downto 0)
        );
end mux;

architecture rtl of mux is
begin
    process (a,b,c,d,sel)
        begin
            case sel is
                when "00" => output <= a ;
                when "01" => output <= b ;
                when "10" => output <= c ;
                when others => output <= d;
            end case;
    end process;
  end rtl;
```

Listing A.8: PISO

```
entity PISO is
    port(
        system_clk              :in std_ulogic;
        enable                  :in std_ulogic;
        data_in                 :in std_ulogic_vector(24 downto 0);
        serial_data_out         :out std_ulogic
    );
end PISO ;

architecture rtl of PISO is
    signal tmp: std_ulogic_vector(24 downto 0):=(others => ’0’);
begin
    process(system_clk)
        begin
```

```
        if rising_edge(system_clk) then
            if enable='1' then
            tmp <= data_in;
            else
            tmp <= tmp(23 downto 0) & '0';
            end if;
        end if;
    end process;
    serial_data_out<= tmp(24);
end rtl;
```

Listing A.9: PISO flag

```
entity PISO_flag is
    port(
        system_clk          :in std_ulogic;
        enable              :in std_ulogic;
        serial_data_out     :out std_ulogic
    );
end PISO_flag ;

architecture rtl of PISO_flag is
    constant flag: std_ulogic_vector(49 downto 0)
                 := "01010101010101010101010101010101010101010101010101";
    signal tmp: std_ulogic_vector(49 downto 0);
begin
    process(system_clk)
        begin
            if rising_edge(system_clk) then
                if(enable='1') then
                tmp <= flag;
                else
                tmp <= tmp(48 downto 0) & '0';
                end if;
            end if;
    end process;
serial_data_out<= tmp(49);
end rtl;
```

Listing A.10: Register

```
entity reg is
    port(
        input           :in std_ulogic_vector(20 downto 0);
        enable          :in std_ulogic;
        clk             :in std_ulogic;
        output          :out std_ulogic_vector(20 downto 0)
    );
end reg;

architecture rtl of reg is
    begin
        process (clk)
            begin
                if rising_edge(clk)and enable='1' then
                output<=input;
                end if;
        end process;
end rtl;
```

Appendix B

Publications

A paper on the UB01 prototype has been presented at the 2017 13th IEEE Conference on Ph.D. Research in Microelectronics and Electronics (PRIME), while a paper on UB33 has been published in the 2018 IEEE International Conference on IC Design & Technology (ICICDT).

The papers are listed in the next pages.

A MOX Gas Sensors Resistance-to-Digital CMOS Interface with 8-bits Resolution and 128dB Dynamic Range for Low-Power Consumer Applications

F.Ciciotti, A. Baschirotto
Department of Physics
University of Milano-Bicocca
Piazza Scienza, 20126 Milano, Italy

C. Buffa, R. Gaggl
RF & Sensors
Infineon Technologies Austria AG
Villach, Austria

***Abstract*—In this paper an interface circuit for MOX gas sensor is presented. It is based on a resistance-to-frequency converter and improves existing solutions in term of performance (offset) and power efficiency. The resistive range covered is 100Ω-1MΩ, with an equivalent 8-bit precision in a total measurement time of 1 second. This corresponds to a dynamic range of about 128dB. Power consumption and design strategy are optimized for mass production targeting consumer applications. The interface is implemented in a standard CMOS 130nm technology with an area of 125000 μm^2 and 450μA of current consumption.**

Keywords—MOX; resistance-to-frequency; converter; sensor interface; MEMS; gas sensors; low-power.

I. INTRODUCTION

Detection of toxic and dangerous gases has always been a need for safety purpose. In recent years, due to an increasing attention to air quality in addition to safety standards, portable and low-cost gas sensing systems are becoming of main interest. Among all technologies and gas sensor topologies, Metal Oxide Semiconductor (MOX) sensors are widely used due to their inherent compatibility with integrated MEMS technologies (cost and power) and long lifetime (5-10 years) [1].

MOX sensors are based on metal-oxide thin films deposited on a silicon substrate. The interaction between gas molecules and the surface of the sensor itself causes a variation of the sensing element, which behaves like an electrical resistance whose value is proportional to the number of adsorbed molecules. Many readout topologies for resistive sensors are present in literature and they can be summarized in three main categories: 1) a direct resistance-to-voltage conversion, based for example on a voltage divider; 2) a multi-scale voltage-readout approach and 3) a resistance-to-frequency conversion [2,3,4]. The direct resistance-to-voltage conversion is the simplest to be implemented but its dynamic range (DR) is limited by the power supply (which is also scaling with technologies). Multi-scale approach and resistance-to-frequency conversions allow a much higher dynamic range and are more suitable to be used with MOX sensors since their resistive variation is quite large. Indeed a MOX resistance can vary over several decades, not only due to gas concertation, but also due to technology spread of the baseline resistance, temperature and aging. Resistance-to-frequency concept can benefit from scaled technologies because of the voltage to time conversion.

In reference [3] a resistance-to-frequency converter based on an oscillator is presented. The current, resulting from biasing the sensing element at a constant voltage, is charging and discharging an integrator capacitance. Integrator output is a triangular wave whose period is proportional to the resistance value. Compared to other solutions based on oscillators [5], MOX resistance has a constant biasing voltage with the benefit not to compromise its performance and linearity. A possible drawback is a high sensor current when the sensing element resistance becomes very small, with consequent power consumptions not compatible with mobile applications. Programmability, used to face a high dynamic range, increases the complexity of this solution (more complex digital control) and its cost in terms of silicon area. The goal of this work is to develop a standard CMOS compatible interface for MOX sensors based on a resistance-to-frequency architecture for consumer applications, focusing on current and area minimization with resolution for mobile applications.

II. MOX SENSOR

MOX sensors are sensitive to different gases depending on operating temperature, typically in the range 200 ÷ 450 °C, reached with embedded integrated heaters. The target gas reacts with sensor surface, changing the electrical conductivity of the sensitive layer (Fig. 1).

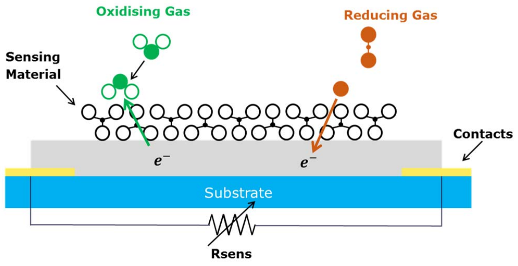

Fig. 1. MOX sensor: a substrate heater is integrated to reach target temperature. Gas adsorption happens at the surface of heated oxide, resulting in a electrical resistance variation.

978-1-5090-6508-0/17/$31.00 ©2017 IEEE

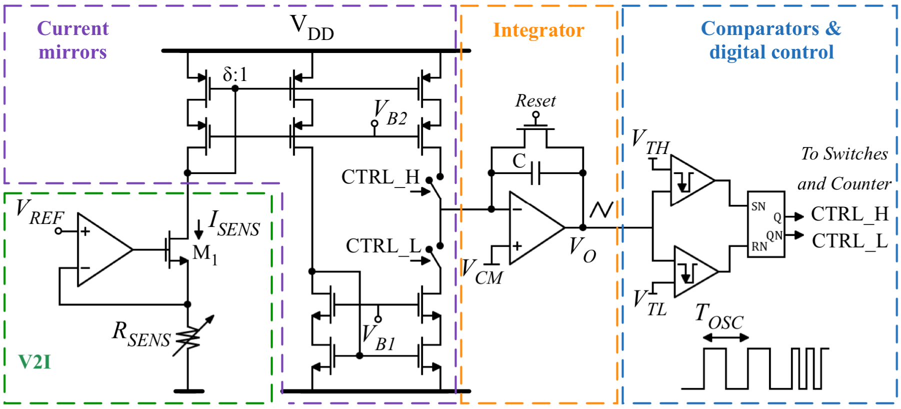

Fig. 2. System architecture of resistance to digital converter

If the reaction occurs with an oxidizing gas, which gains some electrons from the sensitive layer, the overall sensor resistance increases; vice versa, if the adsorbed analyte is a reducing gas, the resistance decreases.

MEMS technology enables miniaturization of MOX sensors and their implementation in a MEMS-CMOS compatible low-cost system.

III. CONCEPT AND SYSTEM DESIGN

A. Overall System Architecture.

The proposed system architecture is shown in Fig. 2: a voltage-to-current (V2I) converter, composed by an OPAMP and transistor M_1, provides a biasing voltage across sensing resistance, R_{SENS}, using a stable reference and bias voltages V_{REF}. Low output resistance at the buffered V_{REF} node is guaranteed by feedback and source follower presence. A current $I_{SENS}=V_{REF}/R_{SENS}$ is then mirrored and alternatively sunk from or sourced in a virtual ground of an integrator, according to control signals CTRL_H and CTRL_L. Integrator output voltage V_O is a triangular waveform which is compared to two reference voltages (V_{TH} and V_{TL}) to generate switches control signals and to steer current. An additional flip-flop always guarantees that comparators switch synchronized. The period of integrator output waveform is proportional to resistance value according to:

$$T_{OSC} = \frac{2C \cdot \Delta V \cdot R_{SENS}}{\delta \cdot V_{REF}} \qquad (1)$$

Where $\Delta V = V_{TH} - V_{TL}$ is comparators switching window and δ is V2I mirrors ratio. Finally, the measurement is carried out in the digital domain by counting how many oscillations occur in a precisely defined time window.

Table 1 reports main system and sensor specifications according to which this concept is developed. The target resolution allows a precision in the gas measurement in the order of magnitude of tens of ppm.

TABLE I. SPECIFICATIONS.

System	
Maximum measurment time	1 s
Resolution	0.4 % (8 bits)
MOX sensor	
Resistance range	100Ω-1MΩ (80dB)
Maximum allowed current	500μA

B. Simulink model, design constraints and specifications.

According to the maximum current allowed through the sensor for power consumption considerations issues, a maximum voltage drop across MOX element of 50mV can be applied considering a worst-case 100Ω resistance. Such a small voltage makes V2I precision very critical. A major advantage of a time-domain approach is that white noise is averaged over the quite long measurement. For the same reason also flicker noise does not affect the overall output count significantly: indeed in the time domain flicker noise behaves similar to thermal noise having a zero average but with higher peak values. On the other hand, every static error impacts and affects measurement precision. At a biasing of 50mV even a small offset of V2I operational amplifier can heavily change signal current value, leading to an incorrect output measurement.

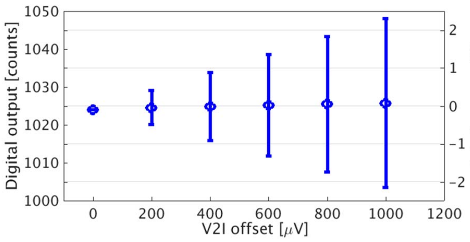

Fig. 3. Simulink model: digital output variation and corresponding error (3σ bars) as a function of V2I offset.

A Simulink model is developed as a proof of concept and to derive ASIC blocks specifications from system requirements. It includes a model of each component with non-idealities (offset, leakage, ...) and noise sources. Design parameters are optimized by the model to meet specifications. Fig. 3 shows a simulation result about offset impact on the final digital output code and its relative error. The measurement time of 1 second is set according to oscillator frequency and system full-scale range. Integrator OpAmp bandwidth requirements and a minimum DC gain are also driven by maximum oscillation frequency, leading to 180MHz and 50dB respectively. The integrator OpAmp in fact must be fast enough to follow the signal output oscillation in the fastest operative mode. Integrator feedback capacitance and current mirrors are optimized to minimize static errors and area.

In order to fulfil a system specification of 0.4% accuracy, a 10-bits resolution design of the counter is chosen to cope with additional errors given by offset in the analog chain. Therefore, the overall number of counter bits is set by DR and by the equivalent desired precision of 10 bits, resulting in:

$$N_{bit} > log_2\left(\frac{R_{max}}{R_{min}}\right) + 10 = 24 \qquad (2)$$

The complete specifications for the system are summarized in table 2.

TABLE II. SUMMARY OF FRONT-END PARAMETERS.

Summary of Front-End Parameters	
V_{REF}	50mV
Integrator capacitance C	3.05pF
Current mirrors ratio (δ)	1:10
Comparator tresholds	$\Delta V = V_{TH}\text{-}V_{TL}$ = 1.2V-0.4V = 0.8V
Counter bits	24

IV. ASIC DESIGN

A. V2I Opamp

To achieve desired resolution, DC gain and output swing without increasing current consumption, a folded cascode topology with p-MOSFET input pair is chosen (schematic in Fig. 4). The large area of input stage transistors M_1 and M_2 (W=300µm L=10µm) and current mirrors, combined with a subthreshold operation, allow reaching a DC gain of 94dB and an offset (1σ) of ≈150µV consuming only 5µA of current from supply voltages in the 1.5V-1.8V range. Solutions to dynamically remove offset, like chopping or auto-zero, are discarded due to their higher consumption and complexity (a single-ended stage has intrinsic asymmetry worsening chopping result).

B. Current Mirrors

The low-voltage cascoded current mirrors are designed to guarantee the desired resolution in all the current sensor dynamic range (500µA-50nA).

To further reduce power consumption and to fulfil system requirements on integrator and comparators, a mirroring ratio δ, 1:10, is used. V2I output current is steered by 2 switches controlled by digital logic.

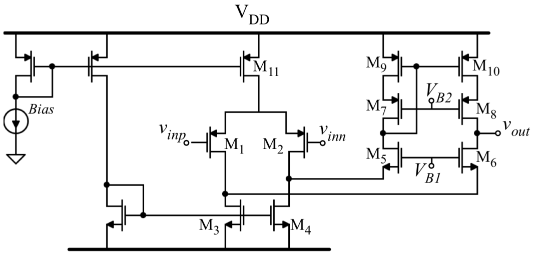

Fig. 4. V2I OpAmp. DC gain: 94dB, I=5µA, φ_m=80°.

C. Miller Integrator and comparators

Integrator OPAMP minimum DC gain (50dB) and bandwidth specifications are derived from system level simulations. Fig. 5 shows measurement error as a function of integrator OPAMP bandwidth. In order to fulfil a system resolution of 8bits, a Unity Gain Band Width (UGBW) of 180MHz corresponding to 0.2% error is needed in worst case of 100Ω sensor resistance. This error sums to V2I error. Despite a single stage topology, like a telescopic, best fits low-power, bandwidth and high DC gain requirements, a folded-cascode opamp is chosen because of output swing. The larger is comparators switching window, the lower is offset impact on output resolution. The designed OpAmp has a DC gain of 55dB and 200MHz of bandwidth using 250µA of current.

Finally, the two continuous time comparators (schematic in Fig. 6) that control current steering switches are optimized for power consumption, with an average current of 80uA each, without lacking of speed (response time < 1ns). For both comparators and integrator, offset is not a critical issue as investigated with Simulink model, due to high output voltage swings, on the other hand, speed can be critical during fast oscillations. The comparators exploit small transistors and a positive feedback loop structure to rise unbalancing speed. The counter has 10 bits resolution not to be a dominant element in system resolution.

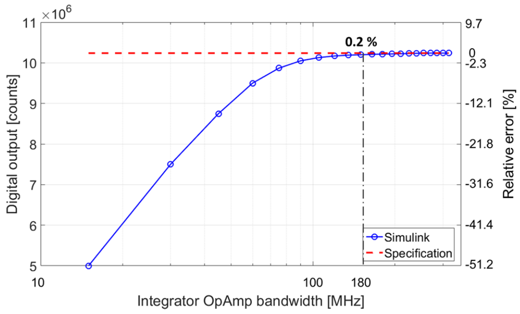

Fig. 5. Simulink model: digital output variation and corresponding relative error as a function of integrator bandwidth. Bandwidth requirements are critical for the lowest sensor resistance value, 100Ω.

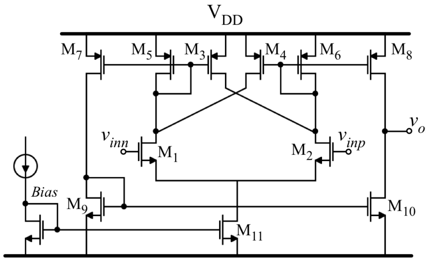

Fig. 6. Continuous time comparator.

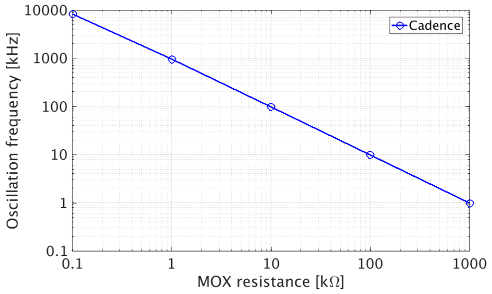

Fig. 7. ASIC simulations: output oscillation frequency vs. input sensor resistance.

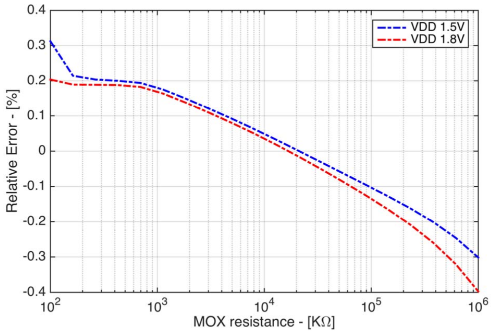

Fig. 8. ASIC simulation: Relative error vs. input sensor resistance for different power supplies.

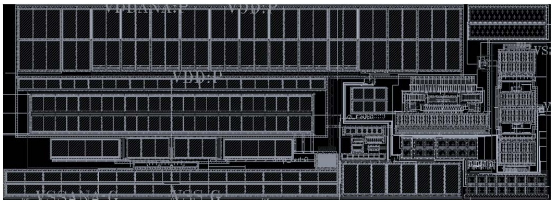

Fig. 9. ASIC Layout

V. PROTOTYPE AND SIMULATION RESULTS

In Fig. 7 and in Fig. 8 simulation results for the ASIC are shown. In Fig. 7, oscillator output frequency is plotted against MOX sensor resistance value for the entire dynamic range, while Fig. 8 shows the associated measurements relative error. The error is within specifications for both possible power supplies, even if a clear trend can be observed: the system is faster in respect with the ideal measurement (negative relative error) when the sensor resistance is very big, and becomes slower and slower (positive relative error) as the sensor resistance decreases. This behavior is mostly due to leakage currents and mirrors inaccuracy that dominates for big R_{SENS} and integrator and comparators speed for small R_{SENS}. The overall current consumption, including biasing blocks, is 450μA, improving by a factor 5x solution proposed in [3]. Additionally has to be accounted the current consumption of sensor branch which depends on gas concentration.

The complete system is implemented in a standard CMOS 130nm process using an area of 125000 μm^2 (chip layout in Fig 9). V2I OPAMP and current mirrors occupy most of the area for offset and matching purposes.

VI. CONCLUSIONS

In this work a versatile resistance-to-digital interface for MOX sensors is presented, providing 128dB dynamic range with 8-bits relative measurement error with a proper system optimization. This solution, intended as an interface for MOX sensors with resistance in the range 100Ω-1MΩ, can be easily adapted to different absolute higher resistance ranges by changing V_{REF}. This is achieved without any programmability, making the system more simple, cheap and robust. Output sample rate is independent of gas concentration. With respect to previous works, power and fabrication spread are optimized making this solution suitable for industrial mass production for consumer applications.

REFERENCES

[1] Yole Developpement, Gas Sensor Technology and Market report, 2016.

[2] J. W. Gardner, P. K. Guha, F. Udrea and J. A. Covington, "CMOS Interfacing for Integrated Gas Sensors: A Review," in *IEEE Sensors Journal*, vol. 10, no. 12, pp. 1833-1848, Dec. 2010.

[3] M. Grassi, P. Malcovati and A. Baschirotto, "A 141-dB Dynamic Range CMOS Gas-Sensor Interface Circuit Without Calibration With 16-Bit Digital Output Word," in *IEEE Journal of Solid-State Circuits*, vol. 42, no. 7, pp. 1543-1554, July 2007.

[4] M. Grassi, P. Malcovati and A. Baschirotto, "A 160 dB Equivalent Dynamic Range Auto-Scaling Interface for Resistive Gas Sensors Arrays," in *IEEE Journal of Solid-State Circuits*, vol. 42, no. 3, pp. 518-528, March 2007..

[5] A. Flammini, D. Marioli and A. Taroni, "A low-cost interface to high-value resistive sensors varying over a wide range," in *IEEE Transactions on Instrumentation and Measurement*, vol. 53, no. 4, pp. 1052-1056, Aug. 2004.

[6] D. Barrettino *et al.*, "A single-chip CMOS micro-hotplate array for hazardous-gas detection and material characterization," *2004 IEEE International Solid-State Circuits Conference (IEEE Cat. No.04CH37519)*, 2004, pp. 312-313 Vol.1.

[7] M. Graf, D. Barrettino, H. Baltes, and A. Hierlemann, CMOS Hotplate Chemical Microsensors. New York: Springer-Verlag, 2007, pp. 87–89.

A Programmable Dynamic Range and Digital Output Rate Oscillator-Based Readout Interface for MEMS Resistive and Capacitive Sensors

F. Ciciotti*, C. Buffa†, R. Gaggl† and A. Baschirotto*
*Department of Physics, University of Milano-Bicocca, Piazza Scienza, 20126 Milano, Italy
†RF & Sensors, Infineon Technologies Austria AG, Siemensstraße 2, Villach, Austria

***Abstract*— this paper presents a low-cost integrated oscillator-based interface circuit for resistive and capacitive readout. The interface is optimized for MOX gas sensor and can cover a very wide resistive range (100Ω-10MΩ) with an equivalent linearity error of 0.4% (8-bit accuracy), corresponding to 148dB of dynamic range (DR). The architecture cancels the parasitic effects of multiplexing, allowing the conversion of a sensor matrix without decreasing resolution and linearity. Moreover, the same interface can measure capacitive sensors and is optimized to convert sensors in the 1pF-2pF range in 100ms with an accuracy of 3.2e-6 (110dB) at 10Hz of data rate. Programmability of output data rate and DR allows compatibility with different sensors and/or resolution requirements. The interface is implemented in a standard CMOS 130nm technology with an area of 130000 μm^2 including biasing blocks and digital synthesis.**

Keywords—MOX; resistance-to-frequency; capacitive; converter; sensor interface; MEMS; gas sensors.

I. INTRODUCTION

The trend in modern consumer electronic is to integrate lots of different sensors (pressure, temperature, gas, humidity, microphones,...) in a single device. Each sensor is based on different physical principles which translate in different electrical quantities to be detected (mainly resistance and capacitance). The readout electronic has to be adapted to each sensor, which implies the design of different analog readout systems, increasing production costs and final devices power consumption. Most sensors for consumer, automotive and industrial applications are either based on a resistance variation or on a capacitance variation measurement. This work focuses on the development of a simple, cheap, low power, CMOS compatible readout interface for both resistive and capacitive sensors for portable gas sensing systems, a typical scenario where several different sensors coexist. The detection of toxic and dangerous gases has in fact become of main interest in recent years, due to an increasing attention to air quality in addition to safety standards. Among all technologies and gas sensor topologies, Metal Oxide Semiconductor (MOX) sensors are the most promising due to their inherent compatibility with integrated MEMS technologies, their low cost, low power consumption and long lifetime (5-10 years) [1]. MOX sensors are based on metal-oxide thin films deposited on a silicon substrate. The interaction between gas molecules and the surface of the sensor itself causes a variation of the sensing element, which behaves like an electrical resistance whose value is proportional to the number of adsorbed molecules. If the reaction occurs with an oxidizing gas, which gains some electrons from the sensitive layer, the overall sensor resistance increases; vice versa, if the adsorbed analyte is a reducing gas, the resistance decreases. A sketch of a typical MOX sensor is shown in Fig. 1. The transduction principle itself has been used for long time, but there are several complications that make the integration of these sensors in a small portable device particularly challenging. The chemical reaction is only possible if the sensor is heated to high temperatures, typically in the range 200÷450 °C, to be reached with embedded integrated heaters. The sensitivity of the metal oxide based materials depends on factors affecting the surface reaction, such as chemical components, surface-modification, temperature and humidity [2]. As a result, the MOX resistance to be measured can vary over several decades, not only because of the variation due to gas concertation, but also because of combinations of the above mentioned phenomena. Thus a reliable portable gas sensing device must include: a matrix of MOX sensors heated at controlled temperatures (the sensitivity of each sensor to a gas depends on the operative temperature); a heater with a few degrees accuracy; a temperature control system; and a humidity sensor to compensate the unavoidable sensitivity variation due to humidity.

The readout interface developed in this work is optimized to sense the resistance of MOX sensors. Moreover the same readout architecture can measure the capacitance of a capacitive sensor, such as a humidity sensor or a pressure sensor, making the proposed interface very versatile and particularly suitable for a portable device with multiple sensors such as a modern smartphone.

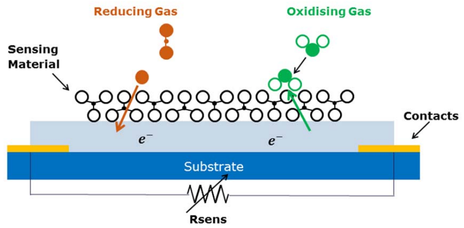

Fig. 1. MOX sensor: the resistance of the sensing layer depends on adsorbed analyte.

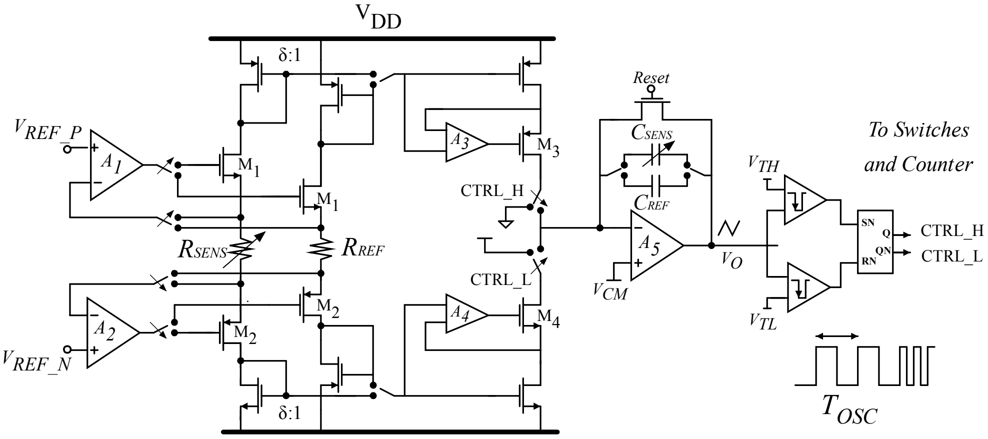

Fig. 2. ASIC architecture: implementation with a 2 channels input stage.

II. THE PROPOSED ARCHITECTURE

A. The resistance-to-frequency conversion principle

Several readout topologies for resistive sensors were presented in the literature, from simple voltage divider to perform direct resistance-to-voltage conversion, to multi-scale approach and resistance-to-frequency conversion systems [3][4][5]. Due to the large resistive range to cover, the direct resistance-to-voltage conversion is not suited for this application since the power supply, which is reducing with technologies scaling, mainly limits the dynamic range (DR). On the other hand, a resistance-to-frequency conversion allows to trade conversion time for resolution and DR, without introducing additional error and complexity typical of multi-scale approaches. Thus, it is the preferred architecture.

In Fig. 2, the schematic of the proposed resistance-to-frequency architecture is reported. It consists of a voltage-to-current (V2I) converter, where two OPAMPs and transistors M_{1-2}, provide a biasing voltage across the sensing resistance, R_{SENS}, using two stable reference and bias voltages V_{REF_P} and V_{REF_N}. The feedback and source follower structure guarantees low output resistance at both buffered V_{REF_N} and V_{REF_P} nodes. The stable biasing at both sensing resistor terminals ensures a better stability of the sensor and isolates it from ground and supply noise. The signal current $I_{SENS} = (V_{REF\_P} - V_{REF\_N}) / R_{SENS}$ is then mirrored and alternatively sunk from or sourced in the virtual ground of an integrator, according to control signals CTRL_H and CTRL_L. At the output of the integrator the voltage V_O is a triangular waveform which is compared to two reference voltages (V_{TH} and V_{TL}) to generate switches control signals and to steer the current. The presence of an additional flip-flop always guarantees the synchronized switching of comparators. The output period waveform is proportional to the sensor resistance value according to the following expression:

$$T_{OSC} = \frac{2C\cdot\Delta V\cdot R_{SENS}}{\delta\cdot V_{REF}} \ , \qquad (1)$$

where $\Delta V = V_{TH} - V_{TL}$ is comparators switching window and δ is the current mirrors ratio. The digital conversion is performed by counting how many oscillations occur in a precisely defined time window.

To use the same interface with a matrix of different sensors, a multiplexed architecture must be implemented. This can drastically affect the system resolution because of the unavoidable parasitic resistance of the multiplexer necessary to select which sensor resistance to measure. The sensor resistance in fact can be as small as 100Ω and the presence of switches R_{on} cannot be neglected. In order to cancel the parasitic effects of the multiplexers they have been connected as shown in Fig. 2. The switches always act on high impedance nodes; thus they do not introduce any additional error.

The MOX interface is optimized to cover the 100Ω-10MΩ range, with a maximum current allowed through the sensor of 500μA limited by the overall power consumption budget. A drawback of this V2I configuration is in fact the high current value reached when the sensing element becomes a smaller resistor. This current limitation leads to a maximum voltage drop across MOX element of only 50mV considering a worst-case 100Ω resistance.

TABLE I. SPECIFICATIONS.

	MOX sensor	**C sensor**
Max Measurment time	2.5 s	100 ms
Target Resolution	0.4 % (8 bits)	18 bits
Resistance range	100Ω-10MΩ	1pF-2pF
Max allowed current	500μA	-
Biasing	Constant Voltage	Constant Current (5μA)

System specification of 0.4% accuracy for R_{SENS} leads to an 8-bits resolution design of the counter, therefore, the overall number of counter bits is set considering DR and the equivalent desired precision of 8 bits, resulting in:

$$N_{bit} > log_2\left(\frac{R_{max}}{R_{min}}\right) + 8 = 25 \quad . \qquad (2)$$

After system level optimization, a compromise between measurement time, maximum oscillation frequency (10MHz), and current consumption has been found. Current mirrors ratio is set to 1:10, integrator capacitance to 3.05pF and comparator switching window to 0.8V. The measurement time is 2.5 seconds for the whole DR. Faster measurements can be performed after the initial estimation of resistance value by reducing the DR covered.

B. The capacitance-to-frequency conversion principle

Eq. (1) indicates that the oscillation frequency of the system depends on both resistance and capacitance value: in the resistance-to-frequency conversion the unknown parameter is R_{SENS}, and the capacitance value is fixed, but it is obviously possible to invert the role of resistance and capacitance and use the same architecture to measure an unknown capacitor. The implemented ASIC allows to disconnect the readout interface from the sensor matrix and to connect it to a reference resistor R_{REF}. A constant current I_{SENS} is then integrated in the sensor capacitance C_{SENS} leading to an oscillation frequency proportional to C_{SENS} itself.

The time domain approach is the best solution to cope the large DR of the MOX resistance (100dB), but can also be effective in the measurement of a capacitance. Typically capacitive sensors have a much smaller variation, but they need a much better resolution than the 8-bit used for MOX resistors measurements. Digital programmability in the control logic allows reconfiguring counters and time window to the C_{SENS} measurements which is optimized to cover the 1pF-2pF range in 100ms. The constant I_{SENS} is set to 5µA, leading to an oscillation period that ranges from 320ns to 640ns. The relative error in C_{SENS} mode is then:

$$\varepsilon_r = \frac{640ns-320ns}{100ms} = 3.2e^{-6} \cong 18.2\ bits \qquad (3)$$

This gives a resolution of ≈ 3.2aF-6.4aF (≈110dB) with a data rate of 10Hz. The resolution increases to ≈130dB decreasing the data rate to 1Hz.

III. ASIC DESIGN

A. V2I Opamps

To achieve desired resolution, DC gain and output swing without increasing current consumption, a folded cascode topology with p-MOSFET input pair is chosen (schematic in Fig. 3) for OPAMPs A_{1-2} in Fig. 2. The large area of input stage transistors M_1 and M_2 (W=300µm L=10µm) and current mirrors, combined with a subthreshold operation, allow reaching a DC gain of 94dB and an offset of ≈150µV consuming only 5µA of current from a 1.8V supply. Solutions to dynamically remove offset, like chopping or auto-zero, are discarded due to their higher consumption and complexity (a single-ended stage has intrinsic asymmetry worsening chopping result). This low offset results in a sufficiently high precision of I_{SENS} in R_{SENS} mode that allows the gas measurement to be performed without the initial calibration usually necessary to compensate static errors in different devices.

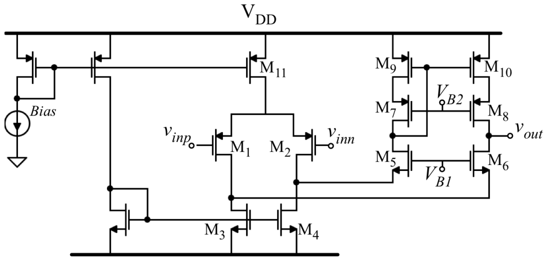

Fig. 3. V2I OpAmps. DC gain: 94dB, I=5µA, φ_m=80° (nominal, 27°C).

B. Current Mirrors

The main challenge in the current mirrors design is to maintain the linearity required in R_{SENS} mode for the entire DR. The mirrors are regulated cascoded to boost their output impedance. Both OPAMPs A_3 and A_4 used in the mirrors structure (Fig. 2) achieve high gains (>90dB) using 5µA current each. They are based on a folded cascoded topology and the only difference between them is that A_3 is a p-input while A_4 the complementary n-input, to better fit the operating point. To achieve robustness, also the design of transistors M_{1-2} and M_{3-4} becomes important. M_{1-2} must have very large W/L (to keep their overdrive low) to avoid saturation of the outputs of amplifier A_{1-2} in high I_{SENS} conditions. M_{3-4} instead must ensure that the outputs of A_{3-4} are always sufficiently separated from VDD and GND, and thus they have a much lower W/L.

The sensor current ranges from 500µA to 5nA and with a mirror ration δ=1:10 to further reduce power consumption. Good linearity in all condition is obtained as highlighted by simulation results reported in Fig. 4, where the mirrors relative error is plotted versus R_{SENS} during PVT variations. It is worth highlighting that in C_{SENS} mode all mirrors linearity problems are much more relaxed, since the current is constant and the C_{SENS} DR is much smaller. The mirrors are set to work in their best nominal operative point.

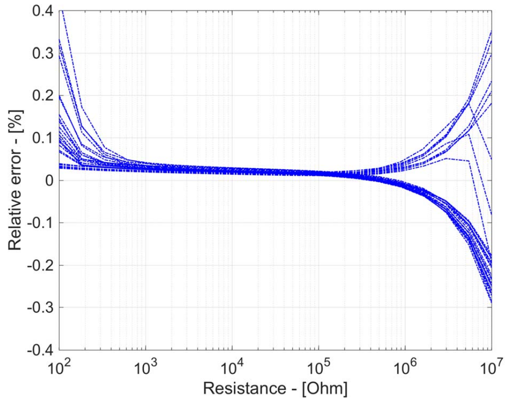

Fig. 4. Current mirrors PVT simulations: relative error vs. input sensor resistance.

C. Miller Integrator and comparators

Integrator OPAMP (A_5) and comparators are the most power hungry part of the architecture because they have to be fast enough during maximum oscillation frequency of 10MHz when R_{SENS} is 100Ω. The OPAMP has 65dB DC gain and 200MHz bandwidth, operating at 250µA. It is based on a classic two-stage miller-compensated architecture, which is particularly suited because of its output current driving and voltage swing capability. The larger is comparators switching window, in fact, the lower is offset impact on output resolution.

The two continuous time comparators (schematic in Fig. 5) that control current steering switches are optimized for power consumption, with an average current of 80µA each, without lacking of speed (response time < 400ps), and they exploit small transistors since having fast response time is more important that low offset. A positive feedback loop is also present to have a small hysteresis. Hysteresis and the presence of a latch guarantee that switches control signals are always properly synchronized.

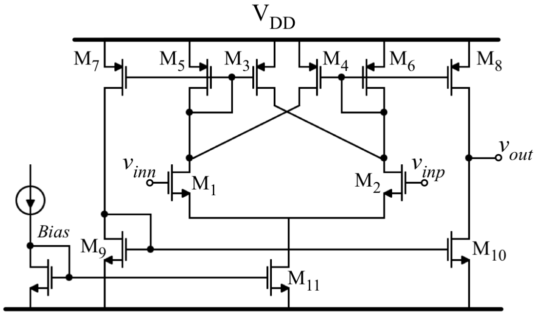

Fig. 5. Continuous time comparator.

IV. PROTOTYPE AND SIMULATION RESULTS

A prototype of the ASIC is implemented in a standard CMOS 130nm process in an area of 0.13 mm^2. The ASIC includes two channels to connect two different MOX sensors and to test system response when switching between channels. Recovery time of current mirrors when disconnecting their gates is negligible compared to the measurement time. Moreover the same circuit can use a reference resistor to convert the readout interface into a capacitive sensors interface. Digital counters and control logic are implemented with the synthesis of VHDL code. The system includes an internal reference oscillator running at 500 kHz. Cadence simulations show that the limiting factor in resolution in R_{SENS} mode is due to the non-linearity of V2I conversion and mirrors (Fig. 4), and in Fig. 6 the output oscillation frequency is plotted versus R_{SENS}. The DR is 148dB with a relative error of ≈ 0.4% or 8-bit for the whole resistive range without performing any kind of calibration. Fig. 6 also shows the output oscillation frequency in C_{SENS} mode in the 1pF-2pF range. Both C_{SENS} and R_{SENS} measurements are almost immune to thermal noise because it is averaged during the long measurement time.

The overall current consumption, including biasing blocks, is 450µA, plus the current consumption of sensor branch which depends on gas concentration, in R_{SENS} mode.

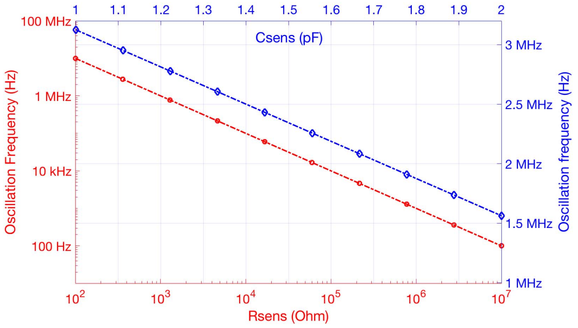

Fig. 6. ASIC simulations: output oscillation frequency vs. input sensor resistance and capacitance.

V. CONCLUSIONS

In this work a programmable interface for resistive and capacitive sensor is presented. The interface is optimized for resistive MOX gas sensors, providing 148dB of dynamic range with an 8-bits relative measurement error, enough to cover the wide resistive range of these sensors. The proposed solution is intended as an interface for MOX sensors with resistance in the range 100Ω-10MΩ and can manage an array of sensors thanks to a smart architecture that eliminates parasitic in the multiplexer. The same interface is also fully compatible with capacitive sensors, and it is optimized to sense capacitive variations of sensors in the 1pF-2pF range in 100ms with 3.2e-6 accuracy. These specifications are common for MEMS capacitive sensors. The possibility to combine resistive and capacitive readout in a single architecture and the versatility of the time domain approach which allows to convert in a digital output virtually any range of resistances and capacitance, makes the proposed interface very versatile and particularly suitable for a portable device with multiple sensors such as a modern smartphone.

REFERENCES

[1] Yole Developpement, Gas Sensor Technology and Market report, 2016.

[2] C. Wang, L. Yin, L. Zhang, D. Xiang, R. Gao, “Metal Oxide Gas Sensors: Sensitivity and Influencing Factors”, in MDPI Sensors, vol. 10, no. 3, pp. 2088-2106, Mar. 2010.

[3] J. W. Gardner, P. K. Guha, F. Udrea and J. A. Covington, "CMOS Interfacing for Integrated Gas Sensors: A Review," in *IEEE Sensors Journal*, vol. 10, no. 12, pp. 1833-1848, Dec. 2010.

[4] M. Grassi, P. Malcovati and A. Baschirotto, "A 141-dB Dynamic Range CMOS Gas-Sensor Interface Circuit Without Calibration With 16-Bit Digital Output Word," in *IEEE Journal of Solid-State Circuits*, vol. 42, no. 7, pp. 1543-1554, July 2007.

[5] M. Grassi, P. Malcovati and A. Baschirotto, "A 160 dB Equivalent Dynamic Range Auto-Scaling Interface for Resistive Gas Sensors Arrays," in *IEEE Journal of Solid-State Circuits*, vol. 42, no. 3, pp. 518-528, March 2007.

[6] A. Flammini, D. Marioli and A. Taroni, "A low-cost interface to high-value resistive sensors varying over a wide range," in *IEEE Transactions on Instrumentation and Measurement*, vol. 53, no. 4, pp. 1052-1056, Aug. 2004.

Bibliography

[1] Yole Developpement, "Gas sensor technology and market report", Tech. Rep., 2016.

[2] "GOSPEL" Network. (). General olfaction and sensing on a european level, funded by european community, [Online]. Available: `http://www.gospel-network.org`.

[3] C. Bur, M. E. Andersson, A. L. Spetz, and A. Schütze, "Detecting volatile organic compounds in the ppb range with gas sensitive platinum gate sic-field effect transistors", *IEEE Sensors Journal*, vol. 14, no. 9, pp. 3221–3228, Sep. 2014. DOI: `10.1109/JSEN.2014.2326693`.

[4] European Environment Agency. (2017). Air quality in europe, [Online]. Available: `https://www.eea.europa.eu/ds_resolveuid/86Y5RVUQT2`.

[5] P. Malcovati, M. Grassi, and A. Baschirotto, "Towards high-dynamic range cmos integrated interface circuits for gas sensors", *Sensors and Actuators B: Chemical*, vol. 179, pp. 301–312, 2013. DOI: `10.1016/j.snb.2012.10.019`.

[6] D. Barrettino, M. Graf, S. Hafizovic, S. Taschini, C. Hagleitner, A. Hierlemann, and H. Baltes, "A single-chip cmos micro-hotplate array for hazardous-gas detection and material characterization", in *2004 IEEE International Solid-State Circuits Conference*, Feb. 2004, 312–313 Vol.1. DOI: `10.1109/ISSCC.2004.1332719`.

[7] J. W. Gardner, P. K. Guha, F. Udrea, and J. A. Covington, "Cmos interfacing for integrated gas sensors: A review", *IEEE Sensors Journal*, vol. 10, no. 12, pp. 1833–1848, Dec. 2010. DOI: `10.1109/JSEN.2010.2046409`.

[8] V. Avramescu, A. D. Luca, M. Brezeanu, S. Z. Ali, F. Udrea, O. Buiu, C. Cobianu, B. Serban, J. Gardner, V. Dumitru, and A. Stratulat, "Cmos-compatible soi micro-hotplate-based oxygen sensor", in *2016 46th European*

Solid-State Device Research Conference (ESSDERC), Sep. 2016, pp. 280–283. DOI: `10.1109/ESSDERC.2016.7599640`.

[9] S. Bedoui, S. Gomri, H. Samet, and A. Kachouri, "Design and electro-thermal analysis of a platinum micro heater for gas sensors", in *2016 13th International Multi-Conference on Systems, Signals Devices (SSD)*, Mar. 2016, pp. 558–561. DOI: `10.1109/SSD.2016.7473712`.

[10] Q. Zhou, A. Sussman, J. Chang, J. Dong, A. Zettl, and W. Mickelson, "Fast response integrated mems microheaters for ultra low power gas detection", *Sensors and Actuators A: Physical*, vol. 223, pp. 67–75, 2015. DOI: `10.1016/j.sna.2014.12.005`.

[11] B. W. H. and B. John, "Surface properties of germanium", *Bell System Technical Journal*, vol. 32, no. 1, pp. 1–41, DOI: `10.1002/j.1538-7305.1953.tb01420.x`.

[12] T. Seiyama, A. Kato, K. Fujiishi, and M. Nagatani, "A new detector for gaseous components using semiconductive thin films.", *Analytical Chemistry*, vol. 34, no. 11, pp. 1502–1503, 1962. DOI: `10.1021/ac60191a001`.

[13] N. Yamazoe and N. Miura, "Some basic aspects of semiconductor gas sensors", in *Chemical Sensor Technology*, S. Yamauchi, Ed., Amsterdam: Elsevier, 1992, pp. 19–42. DOI: `10.1016/B978-0-444-98680-1.50007-3`.

[14] C. Wang, L. Yin, L. Zhang, D. Xiang, and R. Gao, "Metal oxide gas sensors: Sensitivity and influencing factors", *Sensors*, vol. 10, no. 3, pp. 2088–2106, Mar. 2010. DOI: `10.3390/s100302088`.

[15] M. E. Franke, T. J. Koplin, and U. Simon, "Metal and metal oxide nanoparticles in chemiresistors: Does the nanoscale matter?", *Small*, vol. 2, no. 1, pp. 36–50, DOI: `10.1002/smll.200500261`.

[16] N. Barsan, M. Schweizer-Berberich, and W. Göpel†, "Fundamental and practical aspects in the design of nanoscaled sno2 gas sensors: A status report", *Fresenius' Journal of Analytical Chemistry*, vol. 365, no. 4, pp. 287–304, Oct. 1999. DOI: `10.1007/s002160051490`.

[17] A. Heilig, N. Barsan, U. Weimar, M. Schweizer-Berberich, J. W. Gardner, and W. Gopel, "Gas identification by modulating temperatures of sno2-based thick film sensors", *Sensors and Actuators B-Chemical*, vol. 43, no. 1-3, pp. 45–51, Sep. 1997. DOI: `10.1016/S0925-4005(97)00096-8`.

[18] T. A. Kunt, T. J. McAvoy, R. E. Cavicchi, and S. Semancik, "Optimization of temperature programmed sensing for gas identification using micro-hotplate sensors", *Sensors and Actuators B: Chemical*, vol. 53, no. 1, pp. 24–43, 1998. DOI: `10.1016/S0925-4005(98)00244-5`.

[19] D. Meier, J. Evju, Z. Boger, B. Raman, K. Benkstein, C. Martinez, C. Montgomery, and S. Semancik, "The potential for and challenges of detecting chemical hazards with temperature-programmed microsensors", *Sensors and Actuators B: Chemical*, vol. 121, no. 1, pp. 282–294, 2007. DOI: `10.1016/j.snb.2006.09.050`.

[20] K. T. Ng, F. Boussaid, and A. Bermak, "A cmos single-chip gas recognition circuit for metal oxide gas sensor arrays", *IEEE Transactions on Circuits and Systems I: Regular Papers*, vol. 58, no. 7, pp. 1569–1580, Jul. 2011. DOI: `10.1109/TCSI.2011.2143090`.

[21] M. Rossi and D. Brunelli, "Ultra low power mox sensor reading for natural gas wireless monitoring", *IEEE Sensors Journal*, vol. 14, no. 10, pp. 3433–3441, Oct. 2014. DOI: `10.1109/JSEN.2014.2339893`.

[22] R. Huerta, T. Mosqueiro, J. Fonollosa, N. F. Rulkov, and I. Rodriguez-Lujan, "Online decorrelation of humidity and temperature in chemical sensors for continuous monitoring", *Chemometrics and Intelligent Laboratory Systems*, vol. 157, pp. 169–176, 2016. DOI: `10.1016/j.chemolab.2016.07.004`.

[23] C. Falconi, E. Martinelli, C. D. Natale, A. D'Amico, F. Maloberti, P. Malcovati, A. Baschirotto, V. Stornelli, and G. Ferri, "Electronic interfaces", *Sensors and Actuators B: Chemical*, vol. 121, no. 1, pp. 295–329, 2007. DOI: `10.1016/j.snb.2006.09.022`.

[24] E. Sifuentes, O. Casas, F. Reverter, and R. Pallàs-Areny, "Direct interface circuit to linearise resistive sensor bridges", *Sensors and Actuators A: Physical*, vol. 147, no. 1, pp. 210–215, 2008. DOI: `10.1016/j.sna.2008.05.023`.

[25] M. Cole, J. Gardner, A. Lim, P. Scivier, and J. Brignell, "Polymeric resistive bridge gas sensor array driven by a standard cell cmos current drive chip", *Sensors and Actuators B: Chemical*, vol. 58, no. 1, pp. 518–525, 1999. DOI: `10.1016/S0925-4005(99)00130-6`.

[26] D. Barrettino, M. Graf, M. Zimmermann, A. Hierlemann, H. Baltes, S. Hahn, N. Barsan, and U. Weimar, “A smart single-chip micro-hotplate-based chemical sensor system in cmos-technology”, vol. 2, May 2002, pp. II–II. DOI: `10.1109/ISCAS.2002.1010948`.

[27] M. Grassi, P. Malcovati, and A. Baschirotto, “A 160 db equivalent dynamic range auto-scaling interface for resistive gas sensors arrays”, *IEEE Journal of Solid-State Circuits*, vol. 42, no. 3, pp. 518–528, Mar. 2007. DOI: `10.1109/JSSC.2006.891724`.

[28] A. D. Marcellis, A. Depari, G. Ferri, A. Flammini, D. Marioli, V. Stornelli, and A. Taroni, “A cmos integrable oscillator-based front end for high-dynamic-range resistive sensors”, *IEEE Transactions on Instrumentation and Measurement*, vol. 57, no. 8, pp. 1596–1604, Aug. 2008. DOI: `10.1109/TIM.2008.922075`.

[29] M. Grassi, P. Malcovati, and A. Baschirotto, “A 141-db dynamic range cmos gas-sensor interface circuit without calibration with 16-bit digital output word”, *IEEE Journal of Solid-State Circuits*, vol. 42, no. 7, pp. 1543–1554, Jul. 2007. DOI: `10.1109/JSSC.2007.899087`.

[30] Z. Hijazi, M. Grassi, D. Caviglia, and M. Valle, “153db dynamic range calibration-less gas sensor interface circuit with quasi-digital output”, in *2017 New Generation of CAS (NGCAS)*, Sep. 2017, pp. 109–112. DOI: `10.1109/NGCAS.2017.11`.

[31] A. Depari, A. Flammini, D. Marioli, A. Taroni, A. DeMarcellis, G. Ferri, and V. Stornelli, “An uncalibrated wide-range single-supply integrable front-end for resistance and capacitance estimation”, in *TRANSDUCERS 2007 - 2007 International Solid-State Sensors, Actuators and Microsystems Conference*, Jun. 2007, pp. 2031–2034. DOI: `10.1109/SENSOR.2007.4300562`.

[32] A. Depari, A. Flammini, E. Sisinni, A. D. Marcellis, G. Ferri, and P. Mantenuto, “Fast, versatile, and low-cost interface circuit for electrochemical and resistive gas sensor”, *IEEE Sensors Journal*, vol. 14, no. 2, pp. 315–323, Feb. 2014. DOI: `10.1109/JSEN.2013.2282122`.

[33] C. K. Leung and D. M. Wilson, “Integrated interface circuits for chemiresistor arrays”, in *2005 IEEE International Symposium on Circuits and Systems*, May 2005, 5914–5917 Vol. 6. DOI: `10.1109/ISCAS.2005.1465985`.

[34] PRIME Faraday Partnership, *An Introduction to MEMS*, Loughborough University, Ed. Wolfson School of Mechanical and Manufacturing Engineering, ISBN: 1-84402-020-7.

[35] R. Bogue, “Mems sensors: Past, present and future”, *Sensor Review*, vol. 27, no. 1, pp. 7–13, 2007. DOI: `10.1108/02602280710729068`.

[36] A. Dehé, M. Wurzer, M. Füldner, and U. Krumbein, “Design of a poly silicon mems microphone for high signal-to-noise ratio”, in *2013 Proceedings of the European Solid-State Device Research Conference (ESSDERC)*, Sep. 2013, pp. 292–295. DOI: `10.1109/ESSDERC.2013.6818876`.